INTERNATIONAL JOURNAL FOR NUMERICAL METHODS IN FLUIDS, VOL. 23, 753–785 (1996)

NUMERICAL SIMULATION OF THE MECHANISMS GOVERNING THE ONSET OF THE BÉNARD–VON KÁRMÁN INSTABILITY

GILLES CARTE

Institut de Mécanique Statistique de la Turbulence, 12 Avenue du Général Leclerc, F-13003 Marseille, France

JAN DUŠEK

Institut de Mécanique des Fluides de Strasbourg, 2 Rue Boussingault, F-67000 Strasbourg, France

AND

PHILIPPE FRAUNIÉ

LSEET, Université de Toulon et du Var, BP 132, F-83957 La Garde, France

SUMMARY

The onset of the Bénard–von Kármán instability consisting of the selective amplification of the linear unstable mode and yielding finally the well-known saturated state has been described many times on the basis of both numerical and experimental results in various configurations. However, neither the role of the harmonics and their coupling has been examined quantitatively, nor has the spatial structure of the instability been studied in detail. A recently developed numerical method of simulation of quasi-periodic flows makes it possible to integrate the investigation of linear and non-linear characteristics within a single numerical method. The simulation of the 2D afterbody wake presented in this paper allows us to follow the amplification of the instability over many orders of magnitude. It is shown that at all stages of its development the instability is characterized by a series of harmonics, each of them amplified with a multiple of the fundamental amplification rate during the linear regime. The amplification of harmonics results from an energy transfer from the mean flow to harmonics of increasingly higher order. Ultimately the energy losses compensate this transfer and an equilibrium, commonly called saturation of the instability, is reached. It is shown that the coupling between the fundamental harmonic and the mean flow is mainly responsible for the saturation. The convergence rate of the development of the instability into harmonics is investigated. A full description of the spatial structure of all significant harmonics both in the linear regime and at saturation is obtained. The results show that time and space characteristics of the instability can be investigated simultaneously in an efficient way. Such an approach might be particularly important in 3D wakes where the geometry has a strong influence on the behaviour of unstable flows.

KEY WORDS. numerical simulation; spectral time discretization; Navier–Stokes equations; laminar flow; shear flow; unsteady flow; periodic flow; instability; Hopf bifurcation; non-linearity; non-linear theory

1. INTRODUCTION

The investigation and theoretical analysis of instabilities have been the objective of experimental and theoretical studies for several decades. One of the reasons why wakes were mostly focused on[1–5] is their typical Landau-like behaviour characterizing a Hopf bifurcation believed, since Landau,[6] to be

CCC 0271–2091/96/080753–33

Received June 1995
Revised January 1996

at the origin of the transition to turbulence. Other theoretically simple or experimentally realizable configurations were, however, also investigated from the same point of view.[7–10] It has been recognized that a significant amount of information can be obtained from linear theory, but difficulties in solving the linearized Navier–Stokes eigenvalue problem limited linear theory to the parallel Orr–Sommerfeld framework.[2] This framework has been shown to be inadequate for wakes,[11] which explains why, until the pioneering, fully 2D, linear analysis of the onset of the instability in wakes carried out by Jackson,[12] no significant agreement between theory and experiment could be achieved even for such a fundamental characteristic as the critical Reynolds number.

The rapid development of numerical techniques allowing direct resolution of the Navier–Stokes equations has soon made linear theory obsolete by providing a tool for accounting fully for the non-linear effects[3, 13–15] and for supplanting the experimental results in accuracy. In the same way as in other fields of fluid mechanics, direct numerical simulation (DNS) became, however, rather an alternative for experiments than a means of a direct understanding of the described phenomena. The result of this approach to numerical computing was a gap between the theory, which remained at the weakly non-linear level yielding verifiable results only in very special geometrical configurations,[7,8,16] while DNS and increasingly available computing power made simulations of 3D unsteady and even turbulent flows possible. The effort of development of DNS has been too numerically oriented to directly stimulate a better understanding of the non-linear mechanisms described by the solved equations. The main contribution of DNS to the understanding of the non-linear mechanisms in flows lies in their improved accuracy and the possibility to control the boundary conditions and thus eliminate side effects. In the case of the onset of instabilities, DNS thus provided accurate results allowing one to shed light on the details of the fundamental non-linear mechanisms governing the development and saturation of the Hopf bifurcation.[15] Our last numerical and theoretical work[15] drew attention to the physical relevance of the modes of the time Fourier decomposition of the wake and simultaneously unveiled a certain number of serious drawbacks of DNS preventing the study of some theoretically important issues such as the behaviour of the instability at its very onset, the onset of the saturation and the role of coupling of individual modes.

For theoretical purposes it is often useful to reduce the description of the wake to a Landau model with appropriately fitted constants. Experimental papers[4,5,17] attempting to measure these constants showed that the difficulties and errors involved are mainly due to the impossibility of capturing accurately the linear regime (the stage where linear theory applies). This can be explained by the fact that the physically interesting transients related to the instability are overshadowed by experimental transients accompanying the change in experimental boundary conditions. In numerical experiments[15] the transients can be significantly reduced.[3] However, full elimination of the numerical transients is extremely costly and is possible only near the instability threshold. Moreover, it does not allow one to see the higher harmonics which arise from the rounding errors only when saturation is approached.

Recently[18] the importance of the knowledge of the spatial structure of the instability has been recognized. Classical simulation methods can provide access to this structure at saturation; however, the study of its evolution from the linear regime to saturation has been impossible.

In the present paper we give results of a new theoretical approach and a new numerical technique, the principle of which was presented and the numerical properties of which have been analysed in Reference 19. The method allows us to follow the relevant characteristics of the Bénard–von Kármán instability in a continuous way and with high accuracy from the linear regime until saturation. Our method is far more accurate than current direct simulation methods as far as the time dependence is concerned, provides direct access to theoretically relevant entities and allows their detailed study. The principal theoretical issues addressed in this paper are the investigation of the very onset of the instability and the problems of computing the basic flow and of solving the linear instability problem at arbitrary supercritical Reynolds numbers. We also study the generation of higher harmonics, their amplification and structure before the onset of strongly nonlinear effects leading to saturation. The process of saturation is investigated thoroughly from the point of view of amplification rate decrease, angular velocity increase, mode deformation, non-uniformity of local angular velocities and Landau model validity.

From the numerical point of view the very high time discretization accuracy obtained is emphasized. As primarily qualitative aspects were addressed, a relatively poor spatial discretization accuracy was used. The obtained spatial characteristics are, nevertheless, qualitatively in very good agreement with direct simulation results obtained using a highly accurate, experimentally validated, spatial discretization method.[15] From the discussion of this paper it is clear that if high-order harmonics are needed for the sake of the time discretization accuracy or for other purposes, a more accurate spatial discretization is required. The presented numerical method being compatible with a rather wide variety of unsteady Navier–Stokes solvers (time-marching techniques), the implementation of available, highly accurate space discretizations is straightforward.

We consider the presented approach to be particulary promising for the study of secondary instabilities[20] in wakes and thus to be able to provide a deeper understanding of the transition to turbulence.

2. THEORETICAL BACKGROUND

2.1. Governing equations

In our recent paper[15] we pointed out the importance of the Fourier decomposition of the Navier–Stokes equations for the understanding of the onset of the Bénard-von Kármán instability. We shall first explain how a system of equations yielding directly the Fourier modes of the flow is obtained from the Navier–Stokes equations for incompressible and viscous flows in the velocity–pressure formulation

$$\frac{\partial \mathbf{v}}{\partial t} + \mathbf{v}\nabla\mathbf{v} - \nu\nabla^2\mathbf{v} + \nabla p = 0, \tag{1}$$

$$\nabla \cdot \mathbf{v} = 0, \tag{2}$$

where $\mathbf{v}$ is the velocity vector and p is the pressure. These equations have to be completed by boundary and initial conditions, which will be discussed in the next subsection. In this paper we shall be concerned with unsteady flows with a dominant frequency. In this framework a functional approach to the spatial characteristics and the following notation appeared to be useful.[15] The non-linear operator in (1) and (2) will be denoted

$$F(\mathbf{v}) \equiv -\nu\nabla^2\mathbf{v} + \mathbf{B}(\mathbf{v}, \mathbf{v}), \tag{3}$$

where $\mathbf{B}$ is the bilinear operator that accounts for the non-linear contribution of the advective terms and of the pressure:

$$\mathbf{B}(\mathbf{v}, \mathbf{w})_i = v_j \frac{\partial w_i}{\partial x_j} - \frac{\partial}{\partial x_i}(\nabla^2)^{-1} \frac{\partial v_j}{\partial x_k}\frac{\partial w_k}{\partial x_j}. \tag{4}$$

The inversion of the Laplacian operator is equivalent to the usual pressure correction procedure. We use this writing to stress the non-linear role of the pressure term of the Navier–Stokes equation (1). This shorthand notation includes also an appropriate treatment of boundary conditions within the operator (3). We arrive at the following formulation of (1) and (2),

$$\frac{\partial \mathbf{v}}{\partial t} + F(\mathbf{v}) = 0, \tag{5}$$

allowing us to focus on the temporal aspects of the equations. The initial condition (to be discussed later in the case of the onset of in stability in a wake) will be written as

$$\mathbf{v}(0, .) = \mathbf{g}(.). \tag{6}$$

In what follows, the fields of velocity, pressure and their harmonics are considered globally as elements of some functional space defined on the whole computational domain Ω; therefore we suppress all the spatial variables in our notation and replace them by a point.

2.2. *Separation of periodic oscillations*

It is well-known[1,2] that wake are characterized by periodic oscillations. In the transient phase of the onset of a wake, slow transients are superimposed on the periodic behaviour. To separate the periodic oscillations from the transients, let us consider, instead of (5), the equation

$$\frac{\partial \mathbf{u}}{\partial s} + \frac{\partial \mathbf{u}}{\partial t} + F(\mathbf{u}) = 0, \tag{7}$$

where a new time variables s has been introduced. It is clear that if we replace s by t in (7) in the sense $s(t) = t$ and denote

$$\mathbf{v}(t, .) \equiv \mathbf{u}(t, t, .), \tag{8}$$

then $\mathbf{v}$ satisfies equation (5).* As a result, the formulation (7), (8) becomes equivalent to the original Navier–Stokes equations written in the shorthand notation of (5). Now we can assume the t-variable to express the periodicity, i.e. the solution $\mathbf{u}$ is assumed to be (exactly) periodic as a function of t with a given period T:

$$\mathbf{u}(s, t + T, .) = \mathbf{u}(s, t, .). \tag{9}$$

As has been said above, the behaviour of the field $\mathbf{v}$ need not be strictly periodic. The period T is self-generated by the flow and is not given *a priori*; during the development of the instability, the period varies, obeying roughly the Landau model.[6,15] Equation (8) shows that the variable s can account for any deviation of the solution $\mathbf{v}$ of the Navier–Stokes problem (5) from the t-dependence imposed on the solution $\mathbf{u}$. In particular, the s-variable can accommodate non-periodic deviations or deviations from the imposed period. The magnitude of these deviations is quantified by the s-derivative in (7). In principle, the latter may be arbitrarily large; however, the accuracy of the numerical method described below is highest if this term becomes as small as possible.

---

* Equation (8) is a shorthand writing for the composed function relation between the function $\mathbf{v}(t, .)$ of one variable (space variables are not discussed) and the function $\mathbf{u}(s, z, .)$ via $\mathbf{v}(t, .) = \mathbf{u}(s(t), z(t), .)$, where $s(t) = t$ and $z(t) = t$. As a result,

$$\frac{\partial \mathbf{v}}{\partial t} = \frac{\partial \mathbf{u}}{\partial s}\frac{ds}{dt} + \frac{\partial \mathbf{u}}{\partial z}\frac{dz}{dt} = \frac{\partial \mathbf{u}}{\partial s} + \frac{\partial \mathbf{u}}{\partial z}.$$

In equation (7) we denote the z-variable as t.

To obtain a complete mathematical formulation, we add the initial condition

$$\mathbf{u}(0, t, .) = \mathbf{h}(t, .), \tag{10}$$

where $\mathbf{h}(t, .)$ is periodic with the period T introduced in (9) and such that

$$\mathbf{h}(0, .) = \mathbf{g}(.),$$

the field $\mathbf{g}$ being the same as in (6). The initial condition (10) provides the possibility to include an initial guess concerning the periodic behaviour of the solution such as the expansion into harmonics.

2.3. *Fourier decomposition of the periodic behaviour*

The assumed periodicity (9) of $\mathbf{u}(s, t, .)$ as a function of t makes it possible to write the Fourier decomposition

$$\mathbf{u}(s, t, .) = \sum_{n=-\infty}^{\infty} \mathbf{c}_n(s, .)e^{in\omega t}, \tag{11}$$

where $\omega = 2\pi/T$. The developed solution being real, the coefficients of the development (which are functions of s and of the spatial variables) satisfy the relation

$$\mathbf{c}_n(s, .) = \overline{\mathbf{c}_{-n}(s, .)}.$$

The Fourier decomposition (11) inserted into (3), (7) and (10) yields the system of coupled non-linear equations

$$\frac{\partial \mathbf{c}_n}{\partial s} + (in\omega - \nu\nabla^2)\mathbf{c}_n + \sum_{k=-\infty}^{\infty} \mathbf{B}(\mathbf{c}_k, \mathbf{c}_{n-k}) = 0. \tag{12}$$

For theoretical considerations the system (12) presents the advantage of taking account explicitly of the non-linear role of the pressure term via (4). The numerical implementation is based on a straightforward Fourier decomposition of the Navier–Stokes equations (1) and (2). Let us decompose also the pressure into the Fourier series

$$p(s, t, .) = \sum_{n=-\infty}^{\infty} d_n(s, .)e^{in\omega t}, \tag{13}$$

where again $d_n(s, .) = \overline{d_{-n}(s, .)}$. The system (12) can then be written equivalently as

$$\frac{\partial \mathbf{c}_n}{\partial s} + (in\omega - \nu\nabla^2)\mathbf{c}_n + \sum_{k=-\infty}^{\infty} (\mathbf{c}_k \cdot \nabla)\mathbf{c}_{n-k} + \nabla d_n = 0, \tag{14}$$

the Fourier components $\mathbf{c}_n$ satisfying the continuity equation

$$\nabla \cdot \mathbf{c}_n = 0. \tag{15}$$

Except for the non-linear term in (14) and the complex nature of the Fourier components $\mathbf{c}_n$ and d_n, the structure of individual equations (14) and (15) is identical with that of (1) and (2). For this reason the numerical implementation of their resolution requires only minor modifications of a standard Navier–Stokes solver. The number of harmonics accounting with a given accuracy for the time behaviour of an infinite cylinder wake can be assessed from the spectra in Reference 15. It appears that rather high above the instability threshold, five harmonics yield a better than 1% accuracy throughout the whole flow field. Even to reach a high accuracy, it is thus sufficient to truncate the system (14), (15) at a moderate number of harmonics. As we shall see later on, the correct resolution of higher harmonics requires a higher accuracy of the spatial discretization, but the computing effort can easily be optimized and a criterion relating the time and space discretizations can be established.

Moreover, any harmonic can be artificially suppressed, which provides a valuable tool for investigating the role of the non-linear coupling of individual harmonics which has been claimed in Reference 15 to be responsible for the Landau-like behaviour of the wake. The possibility of artificial switching on and off of harmonics provides also a means for an accurate computation of the 'unperturbed' basic flow in an arbitrary configuration and for any supercritical Reynolds number and of solving the linear instability problem.

The initial condition (10) yields, after a Fourier decomposition, initial values $\mathbf{c}_n(0, .)$ of the Fourier coefficients $\mathbf{c}_n$ appearing in (12) and (14). In the context of the instability onset this formulation of the initial condition appears to express best the physics of the problem.

3. NUMERICAL IMPLEMENTATION

In this paper we focus primarily on the physical results. The numerical details of the method used have been given elsewhere[19] and only a brief summary is presented in this section.

3.1. *Modification of the time-marching method*

The numerical implementation of the resolution of (14) and (15) is based on a modification of an implicit finite volume time-marching resolution of the Navier–Stokes equations (1) and (2), second-order-accurate in both space and time, developed by Braza and co-workers.[13,21] The time-marching procedure is now applied to the s-time variable which subsists in the system (14). First- and second-order time discretizations have been considered. For simplicity we present only the first-order version

$$\frac{\mathbf{C}_n^{m+1} - \mathbf{C}_n^m}{\Delta s} + in\omega\mathbf{C}_n^{m+1} + \sum_{k=-\infty}^{k=\infty} (\mathbf{C}_k^{m+1} \cdot \nabla)\mathbf{C}_{n-k}^{m+1} - \nu\nabla^2\mathbf{C}_n^{m+1} + \nabla D_n^{m+1} = 0, \tag{16}$$

$$\nabla \cdot \mathbf{C}_n^{m+1} = 0, \tag{17}$$

where $\mathbf{C}_n^m$ and D_n^m stand for the Fourier components $\mathbf{c}_n$ and d_n discretized in space at the time $s = m\Delta s$, Δs being the s-time step, and ∇ and ∇^2 denote the discretized gradient and Laplacian operators.

To solve the discretized system (17), we introduce the intermediate iteration procedure

$$\frac{(\mathbf{C}_n^m)^{j,*} - (\mathbf{C}_n^m)^j}{\Delta h} + \frac{(\mathbf{C}_n^m)^{j,*} - \mathbf{C}_n^m}{\Delta s} + in\omega(\mathbf{C}_n^m)^{j,*} + \sum_{k=-\infty}^{k=\infty} [(\mathbf{C}_n^m)^j \cdot \nabla](\mathbf{C}_n^m)^{j,*}$$
$$-\nu\nabla^2(\mathbf{C}_n^m)^{j*} + \nabla(D_n^m)^j = 0, \tag{18}$$

$$\nabla^2(\Phi_n^m)^{j+1} = \nabla\cdot(\mathbf{C}_n^m)^{j,*}, \tag{19}$$

$$(\mathbf{C}_n^m)^{j+1} = (\mathbf{C}_n^m)^{j*} - \nabla(\Phi_n^m)^{j+1}, \tag{20}$$

$$(D_n^m)^{j+1} = (D_n^m)^j + \frac{(\Phi_n^m)^{j+1}}{\Delta s}, \tag{21}$$

where $(\mathbf{C}_n^m)^0 \equiv \mathbf{C}_n^m$, $(D_n^m)^0 \equiv D_n^m$, $(C_n^m)^{j_{\max}} \equiv \mathbf{C}_n^{m+1}$ and $(D_n^m)^{j_{\max}} \equiv D_n^{m+1}$, $j_{\max}$ standing for the number of internal iterations.

Equations (18)–(21) are discretized by a second-order finite volume method in space and solved by an ADI algorithm. Δh appearing in (18) is the acceleration parameter of the ADI algorithm chosen as to optimize its convergence. Each internal j-step represents one ADI sweep in both space directions in

(18). Equation (19) is solved by several iterations (not written explicitly) of an ADI Laplace solver to obtain a divergenceless next approximation via (20). The $(j+1)$th internal pressure correction is given by (21). A fixed number of internal steps $j_{\max}$ is chosen to obtain a satisfactory convergence

$$\lim_{j\to\infty}(\mathbf{C}_n^m)^j + \mathbf{C}_n^{m+1}$$

towards the next solution of the external time-stepping procedure (17). At this stage it has to be pointed out that special care has been given to the separation of the physical s-time stepping from the internal ADI iterations. In the original time-marching scheme used to solve unsteady Navier–Stokes problems, the time step Δt has both the role of a physical time step as well as that of an acceleration ADI parameter. The convergence and accuracy are controlled by the size of the time step. In particular, it appears that even if the scheme is, in principle, fully implicit, it may diverge for large time steps. The reason is imperfect matrix inversion. In our case, as we shall see later on, it is important to control the accuracy of the solution of the internal iteration procedure which has been achieved by allowing an arbitrary choice of the number of internal steps. The result is that our procedure converges for a fairly arbitrary time step Δs, typically of the order of one period T.

The convergence with respect to the internal iterations has been analysed in detail in Reference 19. The same numbers of internal steps as those given in Reference 19 are used here. As a matter of fact the accuracy of the internal inversion procedures approaches the machine accuracy, which is certainly not optimal in terms of computing costs. In Reference 19 it is shown that the residual of the equations is reduced to 2×10^{-7}, which is to be compared with 4×10^{-4} obtained with a classical time-marching second-order scheme with a very fine time step. In spite of this, a CPU time reduction as compared with the classical scheme is achieved even with five harmonics taken into account.

3.2. Spatial discretization and configuration

The spatial discretization is based on a finite volume method applied to the Navier–Stokes equations written in their conservative form and integrated over an elementary volume.[13,21] Primitive variables (u, v, p) are discretized on staggered meshes to avoid the numerical problem of the checkerboard instability. A centred discretization of the diffusion term yields a second-order space accuracy.

The configuration and the boundary conditions are presented in Fig. 1. For the sake of numerical simplicity we chose the configuration of an afterbody wake. The wake arises at the inflow of two small 2D channels into a wider one. The flow is the same as that appearing past a long rectangular obstacle placed in the channel. Parabolic channel flow velocity profiles are applied at the inlet. Confined flow between two solid walls (no-slip boundary conditions) is considered. A zero-velocity boundary condition placed symmetrically at the inlet simulates the obstacle. Being steady, these Dirichlet boundary conditions yield zero boundary conditions for all $\mathbf{c}_n$ with $n \neq 0$ and are identical

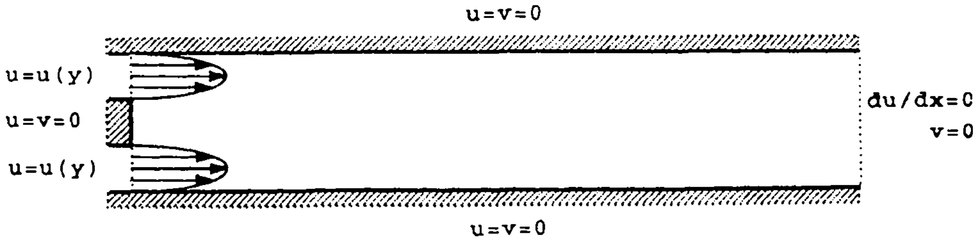

Figure 1. Domain of calculation and boundary conditions

with the boundary conditions for the mean velocity $\mathbf{c}_0$. The outflow boundary conditions are of the Neumann type $\partial \mathbf{c}_n/\partial x = 0$. This unphysical boundary condition is placed sufficiently far downstream so as not to influence the vortex shedding.

The (102 × 32)-point grid used for the simulations is shown in Figure 2. The pressure grid, i.e. the grid whose lines intersect at points where pressure is determined, is represented. The choice of the space discretization method is not optimal in view of the possibilities of the time discretization method used. However, the grid refinement has been tested to be adequate for the Reynolds number considered in what follows. It is sufficient to yield the critical Reynolds number within about 1% accuracy. This means that the basic flow and the fundamental of the instability are resolved accurately enough. Owing to their simple spatial structure, this is not a difficult task. To resolve the higher harmonics is already more difficult. For example, far downstream where the grid is too sparse, the discretization was found inadequate for the fourth and fifth harmonics to be given correctly. However, for the considered Reynolds number, harmonics of order higher than two contribute only about 0·1% even at saturation (see Reference 19 and Section 4.6.1).

3.3. Period correction

In the case of an unsteady wake the period is self-generated, i.e. not exactly known, and it varies in time before the wake reaches saturation. As we have seen, this does not prevent our method from being applicable, the period inaccuracy and variations being accommodated by the s-variable. However, the time discretizations of the s-variations and of the t-dependence are of fundamentally different nature. The t-discretization (the Fourier decomposition) is a spectral one and is thus much more accurate. Actually, we have seen that simulations of an infinite cylinder wake have shown an extremely good accuracy of this discretization. On the other hand, the first- or second-order finite difference s-discretization is far less accurate. To reach the highest possible time accuracy, it is necessary to accommodate the periodic behaviour as exactly as possible in the t-discretization. For this purpose a period correction algorithm adjusting the instantaneous period value at each s-step has been implemented. It is based on a minimization of the s-derivative in (14). For flows with slow transients, such as wakes, this algorithm allows us to reach an extremely high time accuracy.

The principle of the algorithm is based on the fact that for periodic solutions any inaccuracy $\Delta\omega$ in the determination of the angular velocity of the Fourier decomposition (11) results in a rotation of the Fourier components in the complex plane, the angular velocity of the rotation of the Fourier component $\mathbf{c}_n$ being equal to $n\Delta\omega$. The correction of the period even for non-periodic solutions is therefore based on shifting the angular velocity of the harmonics to the Fourier expansion angular velocity ω. The period being exactly uniform throughout the flow and the same for both velocity components and the pressure at saturation and for small amplitudes,[15] any field component at any fixed point in the flow can be used for this purpose. For the sake of accuracy the fundamental

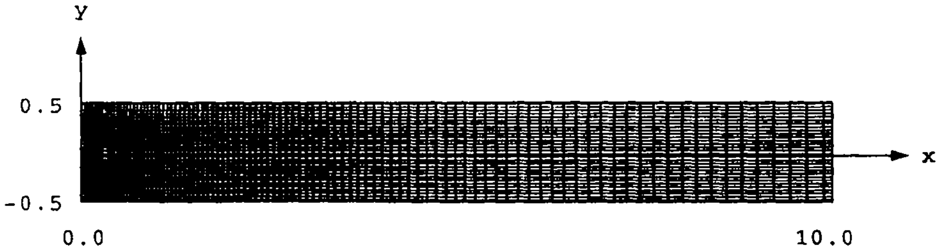

Figure 2. (102 × 32)-point grid used for simulation

harmonic $c_{1,v}$ of the transverse velocity (v) and a point on the flow axis near the maximum of the first v-harmonic have been chosen. At each time step $\Delta\omega$ is calculated from the phase variation of $c_{1,v}$ at the chosen point $\vec{x}_0$ and is used to update ω, so that the value $\omega + \Delta\omega$ instead of ω is used in (17) at the next s-step. The period correction amounts to adjusting the angular frequency of the Fourier expansion in such a way that the phase of $c_{1,v}$ at $\vec{x}_0$ is kept steady:

$$\frac{\partial}{\partial s}\left(\frac{c_{1,v}(s,\vec{x}_0)}{|c_{1,v}(s,\vec{x}_0)|}\right) = 0. \tag{22}$$

This constraint added to (14) and (15) yields the exact, variable angular frequency of the wake.

4. NUMERICAL SIMULATION OF THE INSTABILITY

4.1. *Confined afterbody wake*

The numerical algorithm described above is applied to the study of the development of the Bénard–von Kármán instability in the afterbody wake described in Section 3.2 near the instability threshold. The Reynolds number is based on the bulk velocity ($U_b = 1$) and the width of the obstacle ($D_0 = \frac{1}{3}$). The critical Reynolds number has been found to be about 84 in this case and the value $Re = 90$ has been retained for the flow simulation. The length and velocity scales are made non-dimensional with respect to the domain width $L = 1$ and the bulk velocity $U_b = 1$ respectively.

4.2. *Transient flow simulated with a standard time-marching scheme*

The standard way of simulation of the unsteady wake is the direct numerical solution of (1) and (2). Abundant numerical experience, especially concerning the simulation of the 2D wake of an infinite cylinder,[13–25,22] shows that the instability parameters obtained by this simulation technique are very sensitive to both the spatial and time discretization accuracy. In our case the qualitatively correct behaviour of the wake (onset of vortex shedding) could be obtained with as few as 100 time steps per period using a standard second-order-accurate finite difference time-marching scheme combined with finite volume space discretization. However, to obtain a level of saturation amplitude roughly independent of the time step, $\Delta t = 10^{-3}$ was necessary, yielding approximately 1000 time steps per period.

The experimentally and numerically most frequently investigated flow characteristic in symmetric configurations is the transverse velocity along the flow axis. The reason for this is the absence of the mean value and of even harmonics on the axis for the transverse velocity component.[15] Owing to the rapid convergence of the Fourier decomposition, the signal obtained in this way is almost identical with that of the first harmonic and is thus particularly easy to interpret theoretically.[15] Figure 3 shows the time evolution of the transverse velocity v at the point (1·04, 0·0) on the axis of symmetry of the domain. About 140 periods, corresponding to 140,000 time steps, are represented. For this number of periods it is possible to extract the envelope using the Hilbert transform[23] (see Figure 4). The logarithmic plot of this envelope shows a deviation from the theoretical exponential growth at the beginning of the computation, which is due to numerical transients. As a consequence, the determination of the exponential growth rate characteristic for the onset of the instability is rather difficult to obtain accurately by a direct numerical simulation. The problem of numerical transients is still more serious for the analysis of the time evolution of the angular velocity ω obtained via the Hilbert transform (Figure 5). For very small amplitudes (at the beginning of the simulation) the angular velocity should be roughly constant. Actually, this part of the curve represented in Figure 5 is completely perturbed by numerical transients. The problem of numerical transients is difficult to

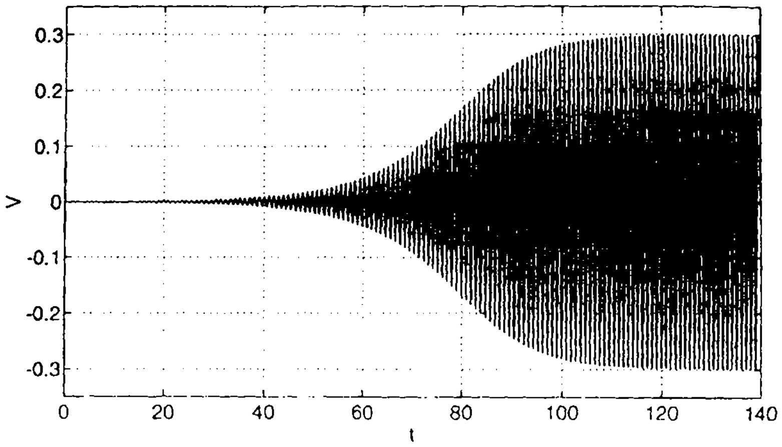

Figure 3. Time evolution of transverse velocity v for calculation with standard time-marching scheme

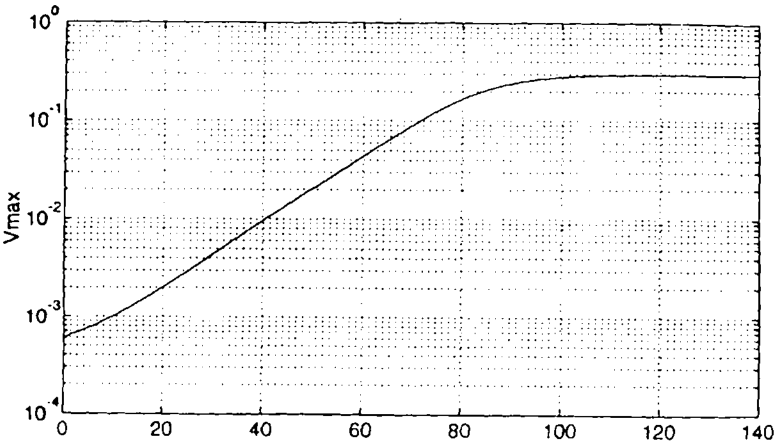

Figure 4. Time evolution of envelope of transverse velocity v for calculation with standard time-marching scheme

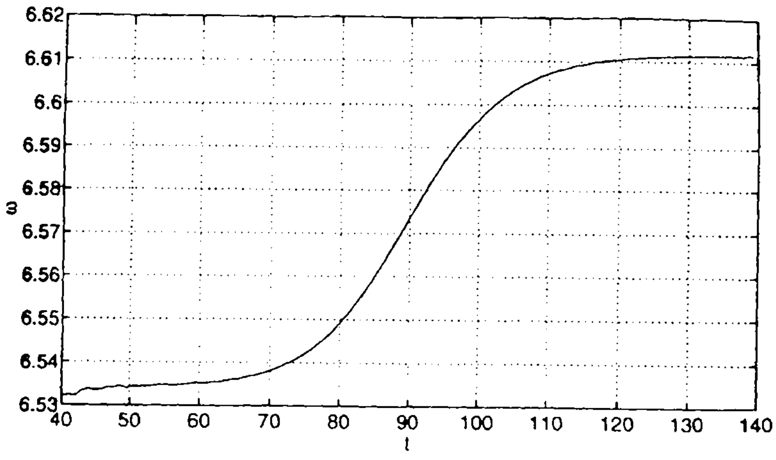

Figure 5. Time evolution of angular velocity ω for calculation with standard time-marching scheme

avoid owing to the rounding errors limiting the number of orders of magnitudes over which the increase can be simulated and owing to the limited physical time of the instability development. This problem is much the same as in an experimental approach and makes the direct numerical solution of the Navier–Stokes equations inadequate for the study of instability parameters higher above the instability threshold.

4.3. Steady solution of the Navier–Stokes equations: basic flow

Let us consider the Navier–Stokes problem defined in Sections 2 and 3 near the critical Reynolds number. For supercritical Reynolds numbers the Navier–Stokes equations describe two steady states: a time-independent one and a periodic one. For subcritical Reynolds numbers the time-independent solution is stable. For supercritical Reynolds numbers it becomes unstable and it is the periodic solution which is stable. This behaviour is characteristic of a bifurcation (a Hopf bifurcation in this case[6]). If a direct Navier–Stokes solver is accurate enough, it reproduces faithfully this behaviour and yields spontaneously the unsteady (periodic) solution at a supercritical Reynolds number. This was the case of the simulation presented in the previous subsection, where numerical noise was sufficient to generate the unsteady flow starting with a rather arbitrary initial condition. The ability to converge to the physically correct values of both existing solutions is a very positive quality of a Navier–Stokes solver; however, it makes the computation of the unstable steady solution, which we shall call the basic flow, difficult. In symmetrical configurations this difficulty can be overcome owing to the symmetry breaking accompanying the Hopf bifurcation. The basic flow even for a highly supercritical Reynolds number can be obtained by forcing the symmetry of the flow that gets broken at the bifurcation.[3] If the configuration presents no symmetry, this trick cannot be used. In this subsection we explain how the basic flow can be obtained by our method.

Let us retain only the (real) mean value terms ($n = 0$) in the Fourier series (11) and (13). It is immediately seen that in this case equations (14) and (15) coincide with (1) and (2). The difference is that we can impose a time step Δs comparable with the Strouhal period of the instability which forces the steady solution of (14) and (15). (In fact a Δs equal to one-tenth of the period does the same job.) The s-variable then assumes the role of a simple relaxation parameter allowing us to start the computation with a rather arbitrary unphysical initial condition. The basic flow solution will be denoted $\mathbf{c}_{0,\mathrm{bas}}$.

The same s-time step can be kept to simulate the whole instability if more terms in the Fourier expansions are kept. This provides a very physical interpretation of this way of computation of the basic flow: the harmonics being blocked, the instability cannot develop.

A typical transverse profile of the resulting (in our case symmetric) basic flow is plotted in Figure 6. It can be seen that the confinement modifies the basic flow rather substantially in comparison with an unconfined wake. The characteristic velocity deficit along the axis responsible for the onset of the instability is, however, clearly visible.

A better way of representing the perturbation of the flow by the obstacle consists of representing the velocity deficit as the difference of the flow without and with the obstacle. In our case

$$\mathbf{c}_{0,\mathrm{def}} = \mathbf{v}_{\mathrm{channel}} - \mathbf{c}_{0,\mathrm{bas}}, \tag{23}$$

where $\mathbf{v}_{\mathrm{channel}}$ stands for the parallel parabolic channel flow profile. The longitudinal velocity deficit and its typical transverse profile are plotted in Figures 7 and 8 respectively. The plot of the flow deficit of the confined wake appears to be very similar to that of an unconfined wake.

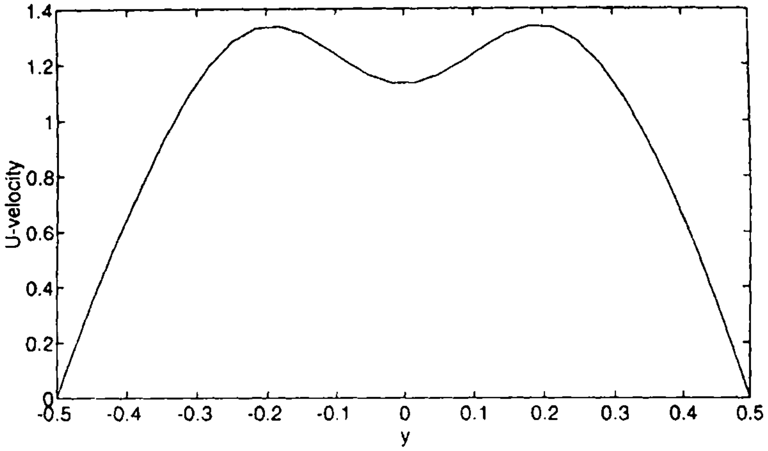

Figure 6. Transverse profile of streamwise u-velocity of basic flow at $x = 4{\cdot}01$

4.4. *Linear instability*

Linear instability theory is based on adding an infinitesimal perturbation to the basic flow determined in the preceding subsection and linearizing the Navier–Stokes equations by dropping the non-linear terms of second order in the perturbation. This approach amounts to keeping only the mean value and the first harmonic (the terms corresponding to $n = 0, \pm 1$) in the Fourier series (11) and dropping the feedback from the first harmonic to the mean flow.

Indeed, if we use the simplified notation (12), we obtain the two equations

$$-\nu\nabla^2\mathbf{c}_0 + \mathbf{B}(\mathbf{c}_0, \mathbf{c}_0) = 0, \tag{24}$$

$$\frac{\partial\mathbf{c}_1}{\partial s} + (\mathrm{i}\omega - \nu\nabla^2)\mathbf{c}_1 + \mathbf{B}(\mathbf{c}_0, \mathbf{c}_1) + \mathbf{B}(\mathbf{c}_1, \mathbf{c}_0) = 0. \tag{25}$$

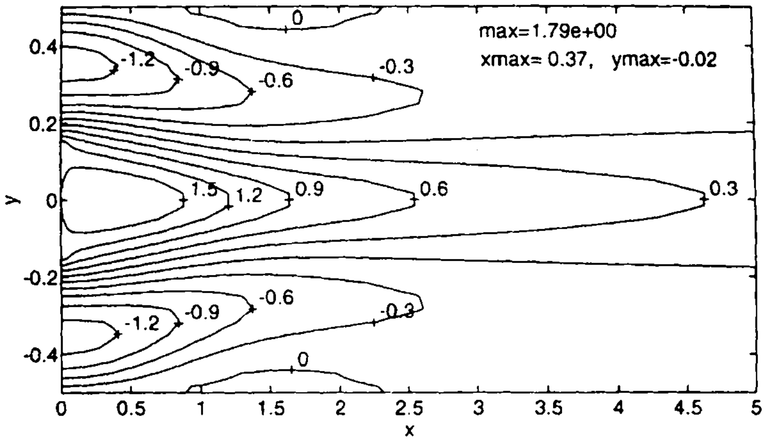

Figure 7. Iso-velocity contours of streamwise u-velocity deficit of basic flow

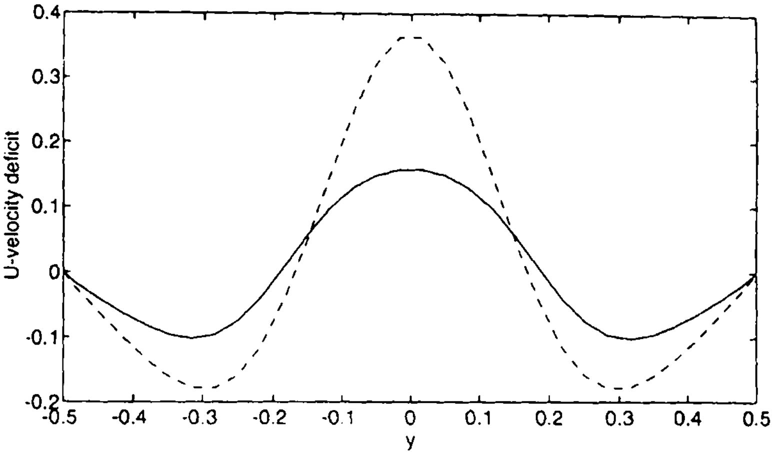

Figure 8. Transverse profile of streamwise u-velocity deficit of basic flow (broken line) and of saturated mean flow (full line) at $x = 4{\cdot}01$

(The equation corresponding to $n = -1$ is obtained as the complex conjugate of (25).) Equation (24) does not contain the coupling with the first harmonic; it is still the (self-contained) equation for the basic flow $\mathbf{c}_{0,\mathrm{bas}}$. Equation (25) coincides with the linearized Navier–Stokes equation for the perturbation $\mathbf{c}_1$ using $\mathbf{c}_0 = \mathbf{c}_{0,\mathrm{bas}}$ as the basic flow. For this reason we shall denote $\mathbf{c}_1 \equiv \mathbf{c}_{1,\mathrm{lin}}$.

The subsystem (24), (25) has been used to compute the solution of the linear eigenvalue problem[15]

$$\lambda \mathbf{c}_{1,\mathrm{lin}} = \mathscr{L}[\mathbf{c}_{0,\mathrm{bas}}]\mathbf{c}_{1,\mathrm{lin}}, \tag{26}$$

where $\mathscr{L}[\mathbf{c}_{0,\mathrm{bas}}]$ is the linear operator (25):

$$-\mathscr{L}[\mathbf{c}_{0,\mathrm{bas}}]\mathbf{c}_{1,\mathrm{lin}} \equiv -\nu\nabla^2\mathbf{c}_{1,\mathrm{lin}} + \mathbf{B}(\mathbf{c}_{0,\mathrm{bas}}, \mathbf{c}_{1,\mathrm{lin}}) + \mathbf{B}(\mathbf{c}_{1,\mathrm{lin}}, \mathbf{c}_{0,\mathrm{bas}}). \tag{27}$$

An arbitrary initial condition for the perturbation $\mathbf{c}_{1,\mathrm{lin}}$ can be taken, because the projections on the subspaces corresponding to stable ($\mathrm{real}(\lambda) \leqslant 0$) eigenvalues decay exponentially whereas the unstable mode is exponentially amplified. The imaginary part of the unstable eigenvalue, $\mathrm{imag}(\lambda) \equiv \omega_0$, is obtained automatically via the period correction procedure described in the previous section as the angular velocity of the truncated 'Fourier decomposition'. The real part ($\mathrm{real}(\lambda) \equiv \gamma$) of the eigenvalue is obtained as the amplification rate (slope of the logarithm) of the solution at an arbitrary point. The relaxation of the projection of the initial solution onto the stable eigenspaces is monitored by letting the amplification rate converge to a fixed value. The obtained solution is normalized by the maximum of the modulus of the transverse velocity component of $\mathbf{c}_1$.

Figures 9 and 11 represent the u- and v-velocity plots showing the spatial structure of the eigensolution of the linear problem. Transverse profiles for both velocity components at a station corresponding to about 10 times the size of the obstacle downstream are plotted in Figures 10 and 12. In spite of the channel confinement and a different basic flow, the spatial structure of the linear mode is very similar to that of the fundamental of the unconfined cylinder wake. The particularity of the present configuration seems to be a more complicated structure of all harmonics near the obstacle, which is probably due to the presence of two mixing layers immediately downstream of the body with sharp edges (e.g. no lateral extrema appear for the transverse component of the fundamental of the unconfined cylinder wake).

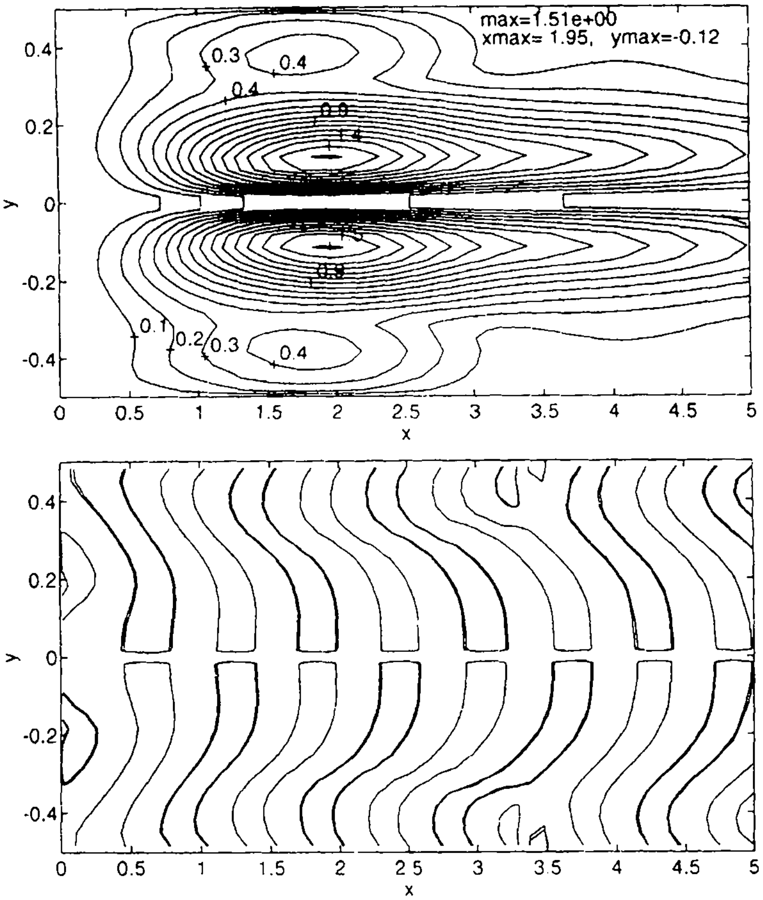

Figure 9. Iso-amplitude (top) and iso-phase (bottom) charts of streamwise component of linear mode. The phase plots are obtained by plotting iso-lines of the real part of the mode divided by the modulus at levels − 0·70, 0·70, 0·75

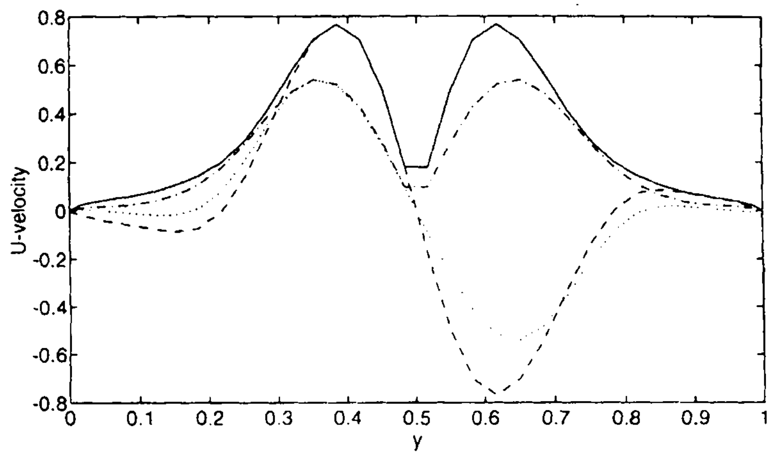

Figure 10. Transverse profile of streamwise component of normalized linear and saturated mode at $x = 4{\cdot}01$: full line, transverse profile of envelope (modulus) of linear mode; broken line, instantaneous transverse profile of linear mode at time when it touches maximum of envelope; chain line, transverse profile of envelope (modulus) of saturated mode; dotted line, instantaneous transverse profile of saturated mode at time when it touches maximum of envelope. The same lines are used to represent the transverse profiles in subsequent figures

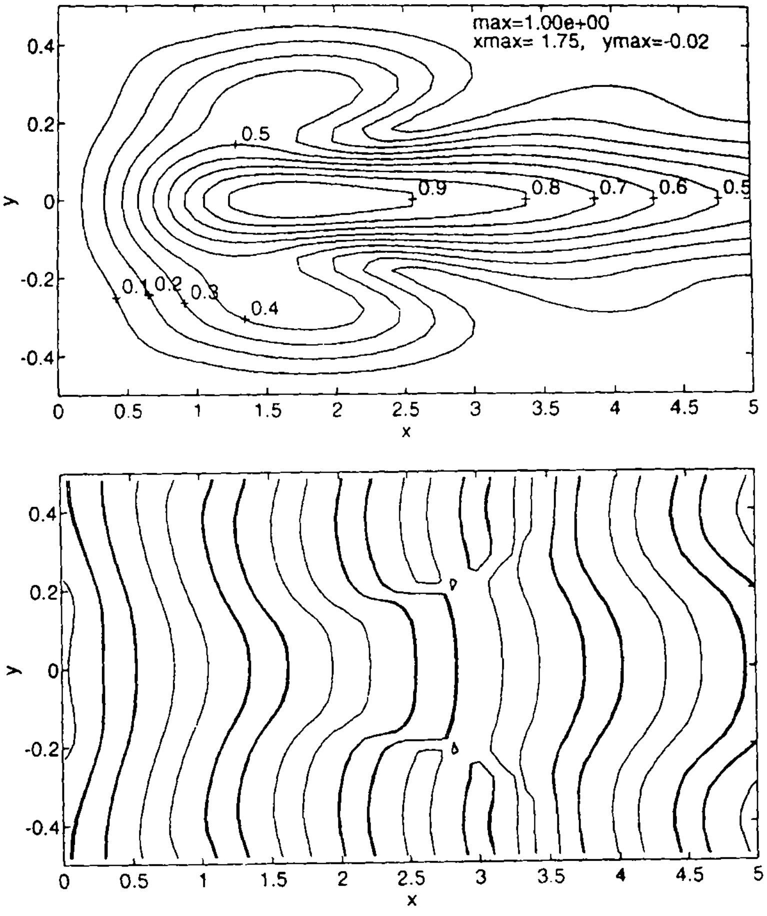

Figure 11. Iso-amplitude (top) and iso-phase (bottom) charts of transverse component of linear mode. The same levels are used for the iso-phase chart as in Figure 9

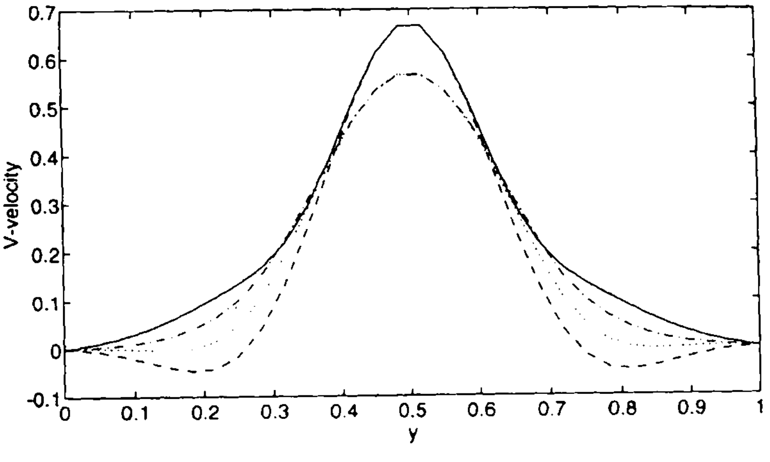

Figure 12. Transverse profile of transverse component of linear and saturated mode at $x = 4{\cdot}01$

At the chosen Reynolds number (90) the eigenvalue of the linear problem was found to be

$$\gamma + i\omega_0 = 0{\cdot}0698 + i6{\cdot}5467. \tag{28}$$

The eigenvalue and the form of the linear mode depend on the configuration in the same way as the critical Reynolds number of the instability does. In the present case the critical Reynolds number was found by interpolation between the amplification rate at $Re = 90$ (28) and at $Re = 80$ ($\gamma_{80} = -0{\cdot}0396$), yielding $Re_{\text{crit}} = 83{\cdot}6$.

4.5. *Slave modes*

In the previous subsection we concluded that the only relevant part of any infinitesimal (linear) perturbation of the steady Navier–Stokes solution is proportional to the linear mode satisfying equations (24) and (25). Owing to the non-linear coupling of the equations of the system (12), the linear mode gives rise immediately to higher harmonics.

Let us denote by ϕ the normalized linear mode represented in Figures 9 and 11:

$$\mathbf{c}_{1,\text{lin}}(s,.) = \alpha e^{\gamma s}\phi, \tag{29}$$

where we split the normalization constant into an exponentially increasing factor and an arbitrary constant α determined by the initial condition. The fact that physically the relevant part of any small initial condition is represented by the mode (29) can be written as

$$\begin{aligned} \mathbf{c}_0(s,.) &\overset{s\to 0}{\sim} \mathbf{c}_{0,\text{bas}}(s,.), \\ \mathbf{c}_1(s,.) &\overset{s\to 0}{\sim} \alpha e^{\gamma s}\phi, \\ \mathbf{c}_n(s,.) &\overset{s\to 0}{\sim} 0 \quad (n \geqslant 2), \end{aligned} \tag{30}$$

the negative indices corresponding to complex conjugates. The infinitesimality of the initial perturbation is expressed by a small value of the constant α.

If we insert the initial condition (30) into the full system (12), we immediately see that terms of higher order in α are generated by the non-linear couplings giving rise to higher-order harmonics. To obtain the order of magnitude of the harmonics, we can introduce a parameter $A(s)$ characterizing the magnitude of the fundamental $\mathbf{c}_1$. For small values this parameter is

$$A(s) \overset{A\ll 1}{\sim} \alpha e^{\gamma s}. \tag{31}$$

Let us renormalize the Fourier components $\mathbf{c}_n$ by introducing

$$\mathbf{a}_n \equiv \frac{\mathbf{c}_n}{A^{|n|}} \tag{32}$$

and let us replace $\mathbf{c}_n$ by the renormalized modes in (12):

$$\frac{\partial \mathbf{a}_n}{\partial s} + \left(|n|\frac{1}{A(s)}\frac{dA(s)}{ds} + in\omega - \nu\nabla^2\right)\mathbf{a}_n + \sum_{k=-\infty}^{\infty} [A(s)]^{|k|+|n-k|-|n|}\mathbf{B}(\mathbf{a}_k, \mathbf{a}_{n-k}) = 0. \tag{33}$$

(The bilinearity of the operator $\mathbf{B}$ was used to factor $A^{|k|}(s)A^{|n-k|}(s)$ out of the non-linear term.) It is easy to see that the exponents in the sum of the non-linear terms in (33) are not negative. Indeed, for $n \geqslant 0$,

$$|k| + |n-k| - |n| = \begin{cases} 0 & \text{if } 0 \leqslant k \leqslant n, \\ 2|k| & \text{if } k \leqslant 0, \\ 2(k-n) & \text{if } k \geqslant n. \end{cases}$$

As a result, the renormalized modes $\mathbf{a}_n$ are of the same order as the small parameter $A(s)$, the leading terms being obtained by truncating the infinite sum in (33) to $0 \leqslant k \leqslant n$ for positive n and $0 \geqslant k \geqslant n$ for negative n. For $n \geqslant 0$ and $A \ll 1$ we thus have

$$\frac{\partial \mathbf{a}_n}{\partial s} + [n(\gamma + i\omega_0) - \nu\nabla^2]\mathbf{a}_n + \sum_{k=0}^{n} \mathbf{B}(\mathbf{a}_k, \mathbf{a}_{n-k}) \overset{A\ll 1}{\sim} 0. \tag{34}$$

The system (34) is recursive. For $n = 0$ it is of course still the basic flow equation, because $\mathbf{a}_0 \sim \mathbf{c}_{0,\mathrm{bas}}$, and for $n = 1$ we obtain the eigenvalue equations (26) and (27). For $n \geqslant 2$, equation (34) can be written as

$$\frac{\partial \mathbf{a}_n}{\partial s} + \{n(\gamma + i\omega_0) - \mathscr{L}[\mathbf{c}_{0,\mathrm{bas}}]\}\mathbf{a}_n + \sum_{k=1}^{n-1} \mathbf{B}(\mathbf{a}_k, \mathbf{a}_{n-k}) \overset{A\ll 1}{\sim} 0, \tag{35}$$

where $\mathscr{L}$ stands for the linear operator (27). The only eigenvalue having a positive real part being $\gamma + i\omega_0$, the operator in braces on the LHS of (35) is certainly non-singular and each equation (35) thus has a unique solution. The basic flow being steady and the time dependence of the linear mode being included in the normalization factor $A(s)$, the first two renormalized modes are steady ($\partial\mathbf{a}_0/\partial s \sim 0$ and $\partial\mathbf{a}_1/\partial s \sim 0$) for small amplitudes. This implies that all renormalized modes are asymptotically (for $A \ll 1$) steady and satisfy the recursion relation

$$\mathbf{a}_0 \overset{A\ll 1}{\sim} \mathbf{c}_{0,\mathrm{bas}}, \tag{36}$$

$$\mathbf{a}_1 \overset{A\ll 1}{\sim} \phi, \tag{37}$$

$$\{n(\gamma + i\omega_0) - \mathscr{L}[\mathbf{c}_{0,\mathrm{bas}}]\}\mathbf{a}_n + \sum_{k=1}^{n-1} \mathbf{B}(\mathbf{a}_k, \mathbf{a}_{n-k}) \overset{A\ll 1}{\sim} 0, n \geqslant 2 \tag{38}$$

The higher Fourier components ($n \geqslant 2$) thus have the following characteristics as long as the fundamental $\mathbf{c}_1$ remains small.

1. Their time dependence is given by that of the fundamental. In this sense they can be considered as slave modes.[9]
2. Their form is time-independent (given by (36)–(38)).
3. The nth mode is amplified exponentially with an amplication rate equal to n times the amplification rate of the fundamental.

We note that the whole renormalization procedure contains the (so far undetermined) normalization constant α which can be chosen arbitrarily. The amplitude value of the fundamental harmonic of an arbitrary flow field component at any fixed point where the amplitude is non-zero can be used. The linear mode being rigid, this choice is equivalent to taking the maximum value of the modulus of a chosen flow field component (u or v) or to taking the greater of the two maxima. In this paper we chose to set α equal to the maximum of the modulus of the transverse velocity component of the linear mode (25):

$$\alpha = \max_{\vec{x}\in\Omega} |\mathbf{c}_{1,\mathrm{lin},v}(0, \vec{x})|.$$

As a result, the maximum of the normalized v-component of the eigensolution ϕ of (26) is set equal to unity.

The parameter $A(s)$ has the role of an order parameter of the Hopf bifurcation. The latter is described non-trivially by an infinite system of modes whose amplitude and form vary owing to non-linear effects as a function of $A(s)$. For small values of $A(s)$ the amplification of the instability is, however, very simple, as described by (31) and (32).

The amplification rates and the orders of magnitude of the slave modes found above can be deduced by perturbation methods.[8] Perturbation theory is, however, difficult to implement for the computation of the slave modes themselves and has not to our knowledge been applied to other than parallel flows.[8] The verification of the theory and computation of the forms of the slave modes by a direct numerical solution of the Navier–Stokes equation is also difficult. This difficulty results not only from the necessity to follow the onset of the instability from a very small perturbation but also from the fact that filtering of higher harmonics from the complete signal would require the level of the numerical noise to be below the level of the highest resolved harmonic (and we have just seen that the magnitude of the *n*th harmonic is proportional to the *n*th power of the fundamental one). The separation of individual harmonics by our method makes this investigation numerically very easy. The renormalization procedure (32) has not been implemented in our code. Nevertheless, we obtain the correct exponential amplification rate over several orders of magnitudes until saturation (Figure 13 and Table I). Figure 13 proves that the renormalization (32) leads indeed to time-independent

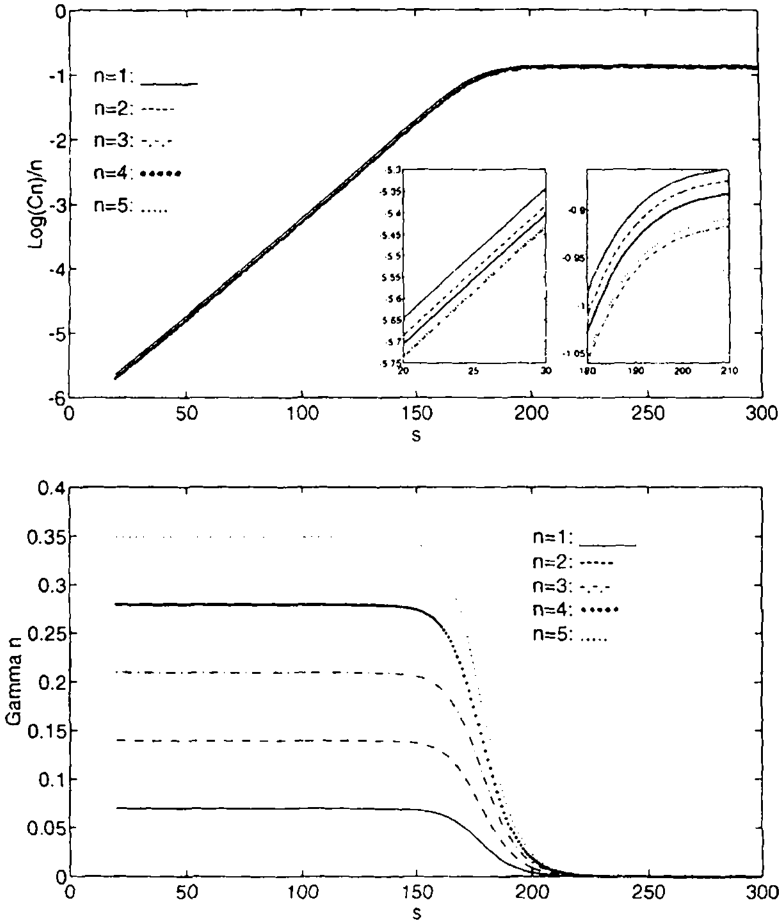

Figure 13. Comparison of amplification rates of five lowest harmonics. Logarithms of the first, third and fifth *v*-velocity harmonics and second and fourth *u*-velocity harmonics at the point $x = 1\cdot 04$ on the flow axis divided by *n* are represetned in the top figure, showing that in the interval characterized by constant amplification rates (small amplitude) the latter are proportional to the order of the harmonic. In the bottom figure the amplification rates themselves are represented

Table I. Amplification rates of each harmonic and their comparisions with amplification rate of fundamental harmonic ($\tilde{c}_{0,u} = c_{0,u} - c_{0,u,bas}$)

	$\tilde{c}_{0,u}$	$c_{1,u}$	$c_{3,u}$	$c_{4,u}$	$c_{5,u}$	
γ_n	0·1395	0·0698	0·1396	0·2095	0·2793	0·3492
$\lvert\gamma_n - n\gamma_1\rvert/n\gamma_1$	$7{\cdot}7 \times 10^{-4}$*	0	$9{\cdot}2 \times 10^{-8}$	$1{\cdot}3 \times 10^{-7}$	$1{\cdot}0 \times 10^{-7}$	$1{\cdot}4 \times 10^{-7}$

*$n = 2$

functions. The forms of the slave modes have been obtained by an *a posteriori* normalization of the solution of the system (14), (15) in the interval of time corresponding to a very low level (10^{-5}) of the order parameter $A(s)$. At this level of the order parameter the non-linear corrections in (33) are of the order of $A^2 = 10^{-10}$ and are numerically imperceptible. The amplitude and iso-phase charts of several lowest-order slave modes are plotted in Figures 14, 16 and 18. The transverse profiles appear in Figures 15, 17, and 19 (full and broken lines).

It is not the purpose of this paper to discuss the details of the spatial structure of the instability. We only note that the higher slave modes have a structure similar to that of the higher harmonics of an

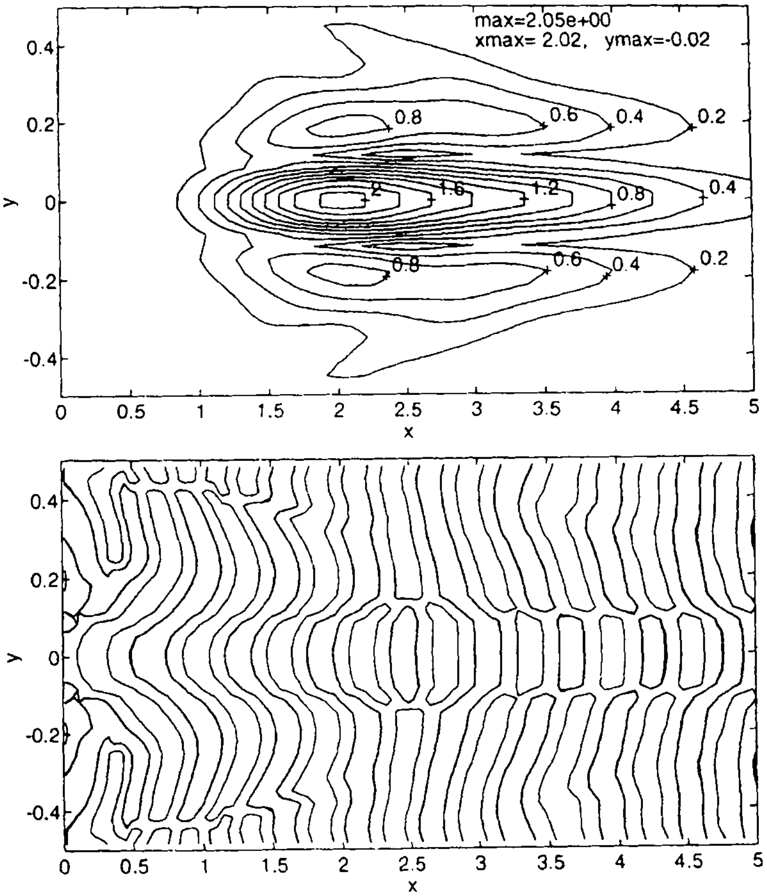

Figure 14. Iso-amplitude (top) and iso-phase (bottom) charts of u-velocity component of second ($n = 2$) slave mode normalized via (32) with A equal to maximum of v-velocity component of fundamental. The levels for representing the phase factor of the second harmonic are −0·5, 0·4, 0·6

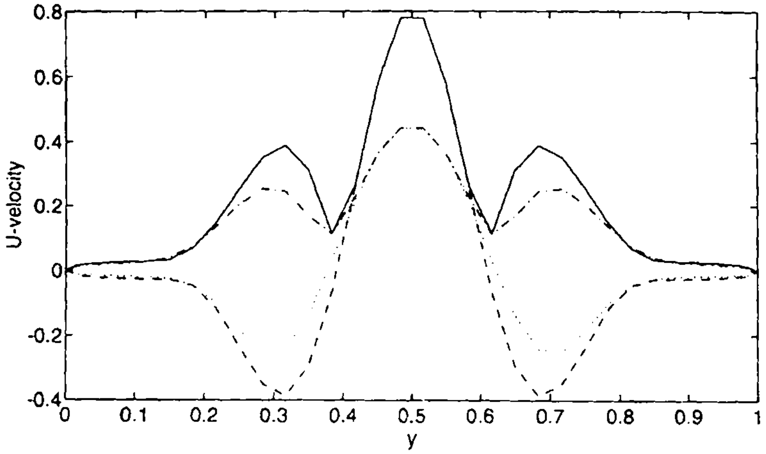

Figure 15. Transverse profile at $x = 4{\cdot}01$ of u-velocity component of second ($n = 2$) slave and saturated mode normalized via (32) with A equal to maximum of v-velocity component of fundamental

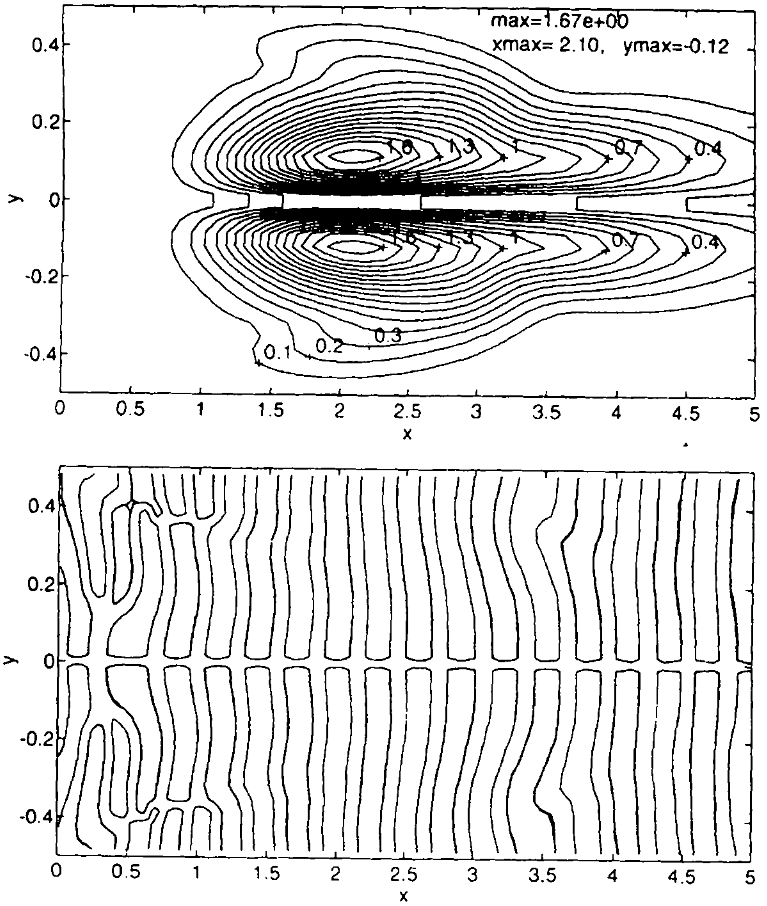

Figure 16. Iso-amplitude (top) and iso-phase (bottom) charts of v-velocity component of second ($n = 2$) slave mode. For normalization see caption of Figure 14

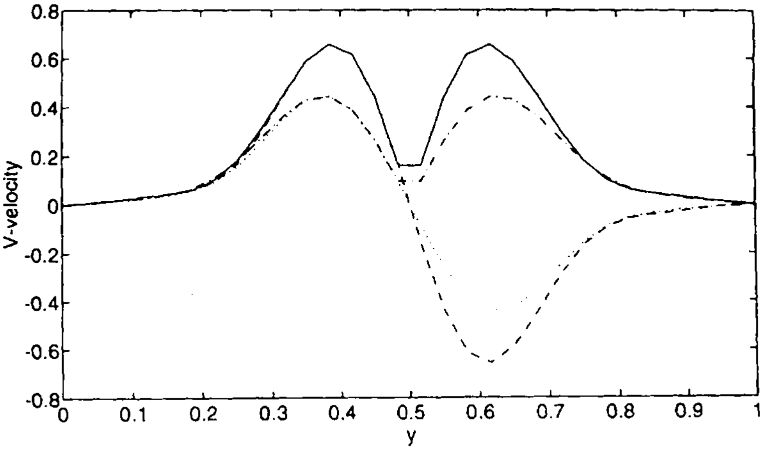

Figure 17. Transverse profile at $x = 4{\cdot}01$ of v-velocity component of second ($n = 2$) slave and saturated mode. See caption of Figure 10

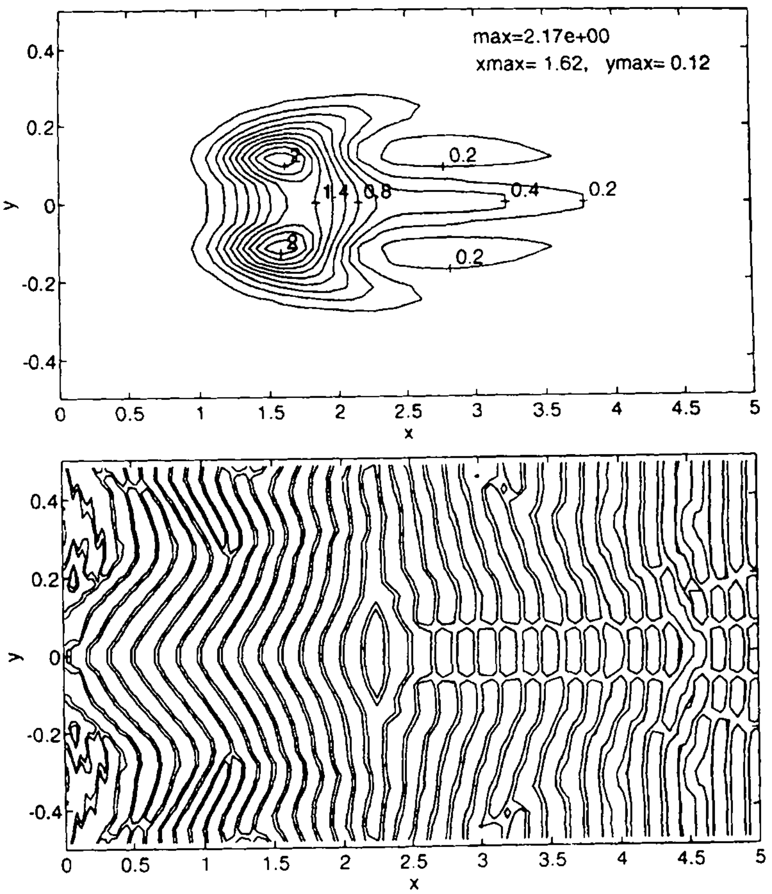

Figure 18. Iso-amplitude (top) and iso-phase (bottom) charts of u-velocity component of fourth ($n = 4$) slave mode. For normalization see caption of Figure 14

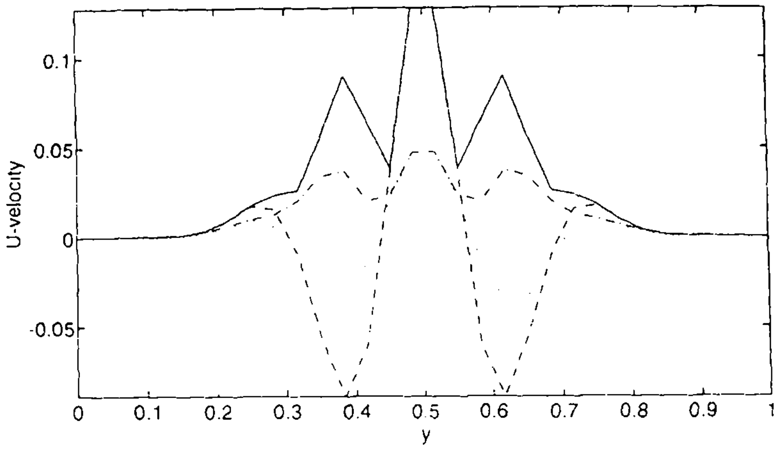

Figure 19. Transverse profile at $x = 4{\cdot}01$ of u-velocity component of fourth ($n = 4$) slave and saturated mode. See caption of Figure 10

unconfined cylinder wake; in particular, the transverse profiles of the modes farther downstream of the obstacle (where the influence of the sharp edges no longer dominates) have the typical character with n extrema for the v-velocity component and $n + 1$ extreme for the u-velocity one.

4.6. *Non-linear effects and saturation*

In the previous subsection we have analyzed the phenomena characterizing the very onset of the instability if it is generated by a very small perturbation. This phase of the instability development is characterized by an exponential growth of all harmonics, the form of which remains rigid. It has also been shown that the size of harmonics is proportional to a power of the (small) order parameter which makes the Fourier decomposition (11) converge very rapidly. As a consequence, the non-linear effects expressed in (33) are negligible. This leads to the decoupling of the system (33) into the recursion (36)–(38). The recursive nature of the system (38) is due to a one-way transfer of energy from the lower harmonics to the higher ones and to negligible energy losses at the lower harmonic levels resulting from this transfer as long as the higher harmonics are much smaller than the lower ones. In this case the system (38) yields exponentially amplified harmonics, the amplification rate of the nth harmonic being n times greater than that of the fundamental. During amplification the higher harmonics thus end up by reaching the same level as the lower ones, which triggers the non-linear effects via the higher-order terms in (33).

The most important consequence of the coupling of harmonics is the transition to saturation. To simplify our analysis, let us drop all therms of order higher than two in (12). Let us define the renormalization factor (32) as

$$A(s) = \max_{\vec{x}\in\Omega} |\mathbf{c}_{1,v}(s,\vec{x})|, \tag{39}$$

i.e. $A(s)$ stands for the spatial maximum of the modulus of the v-component of the fundamental. With the onset of non-linearities the modes start to deform and the s-dependence of the parameter $A(s)$ is no longer independent of the position. There is of course no *a priori* preference for the choice (39). Our choice is made consistently with the previous subsection.

The onset of saturation appears more explicitly if we consider only second-order effects in (12). Dropping all components and terms of order higher than A^2 amounts to truncating the system at $n = 2$

(Equation (32) implies that all higher harmonics are of higher order.) The renormalized system (33) then yields a closed system of three coupled equations

$$\frac{2}{A(s)}\frac{\mathrm{d}A(s)}{\mathrm{d}s}\tilde{\mathbf{a}}_0 + \frac{\partial \tilde{\mathbf{a}}_0}{\partial s} - \mathscr{L}[\mathbf{c}_{0,\mathrm{bas}}]\tilde{\mathbf{a}}_0 + [\mathbf{B}(\mathbf{a}_1, \overline{\mathbf{a}_1}) + \mathbf{B}(\overline{\mathbf{a}_1}, \mathbf{a}_1)] = 0, \tag{40}$$

$$\frac{1}{A(s)}\frac{\mathrm{d}A(s)}{\mathrm{d}s}\mathbf{a}_1 + \frac{\partial \mathbf{a}_1}{\partial s} + (\mathrm{i}\omega - \mathscr{L}[\mathbf{c}_{0,\mathrm{bas}}])\mathbf{a}_1 + [A(s)]^2[\mathbf{B}(\mathbf{a}_2, \mathbf{a}_1) + \mathbf{B}(\mathbf{a}_1, \mathbf{a}_2) + \mathbf{B}(\tilde{\mathbf{a}}_0, \mathbf{a}_1) + \mathbf{B}(\mathbf{a}_1, \tilde{\mathbf{a}}_0)] = 0, \tag{41}$$

$$\frac{2}{A(s)}\frac{\mathrm{d}A(s)}{\mathrm{d}s}\mathbf{a}_2 + \frac{\partial \mathbf{a}_2}{\partial s} + (2\mathrm{i}\omega - \mathscr{L}[\mathbf{c}_{0,\mathrm{bas}}])\mathbf{a}_2 + \mathbf{B}(\mathbf{a}_1, \mathbf{a}_1) = 0, \tag{42}$$

where $\mathbf{a}_0 \equiv \mathbf{c}_0$ and we have introduced the mean flow correction

$$\mathbf{c}_0 = \mathbf{c}_{0,\mathrm{bas}} + A^2(s)\tilde{\mathbf{a}}_0 \tag{43}$$

and the linear operator (27). (The mean flow correction being of the order of A^2, it is convenient to renormalize it by extracting the factor A^2.) This system has to be completed by the period correction equation (22),

$$\frac{\partial}{\partial s}\left(\frac{a_{1,v}(s, \vec{x}_0)}{|a_{1,v}(s, \vec{x}_0)|}\right) = 0 \tag{44}$$

and equation (39), yielding

$$\max_{\vec{x}\in\Omega} |\mathbf{a}_{1,v}(s, \vec{x})| = 1, \tag{45}$$

so that enough equations are given to determine the additional scalar functions $A(s)$ and $\omega(s)$.

At the onset of the instability the parameter $A(s)$ is exponentially increasing according to (31); as a consequence, equation (41) contains a rapidly growing second-order term. As a result of the amplification of the fundamental harmonic expressed by $A(s)$, the second-order term on the LHS of (41) will cease to be negligible. This term can be interpreted as a coupling of the higher harmonics with the lower ones. Indeed, it contains a direct coupling with the second harmonic and a coupling with the mean flow correction $\tilde{\mathbf{a}}_0$ resulting itself as a feedback from the first harmonic to the mean value. As has been shown in Reference 15, the truncated system (40)–(42) is sufficient to obtain the Landau model. In particular, this implies (see also Section 4.6.3) that the effect of this second-order term consists of slowing down the amplification and leading ultimately to a steady value of $A(s)$.

The complete description of the instability is given by the full system (33), (39), (44), (45). In Section 4.5 we have seen that the exponential amplification and rigidity of the slave modes were explained by the recursive nature of the system (38) (obtained by neglecting the energy losses of lower harmonics due to the transfer of energy to higher ones). The growth of higher-order terms in (33) makes it necessary to account accurately for the energy balance between the harmonics by taking into account the inverse couplings in the same way as in the truncated system (40)–(42). As a result, each harmonic ($n = 1, 2, \ldots$) receives energy from the lower ones and the mean value ($n = 0$) and transfers energy to the higher ones. This ultimately brings about an equilibrium state (saturation). At saturation the amplitudes of all harmonics become steady and $A(s)$ and the angular frequency ω reach fixed values. The alternative systems (12) or (14), (15) or (33), (39), (45) completed by the period correction equation (22) thus become steady. In other words, the saturated wake oscillates with a uniform angular frequency throughout the flow with amplitudes and phases described by time-independent Fourier coefficients (11).

The advantage of our computing method lies in the ability to investigate directly the size and form of individual harmonics and analyse the effects of their coupling.

4.6.1. Slave modes and saturated modes. The total deformation of modes due to non-linear couplings can be seen by comparing the spatial amplitude envelopes of the infinitesimal modes with the corresponding saturated modes represented in Figures 20–23. At the selected, only slightly supercritical, Reynolds number the deformation effects are not very strong; however, they are visible. As far as the mean velocity deficit is concerned, Figures 7, 20 and 8 show clearly that it is reduced by the non-linear effects as a result of the transfer of energy of the mean flow to higher harmonics. This reduction is particularly strong near the maximum of the instability (between $x = 1{\cdot}5$ and 2). The global trend of the forms of higher harmonics is characterized by a squeezing in the streamwise direction (Figures 11, 18, and 21–23 and Table II). In the transverse direction the width of the modes remains approximately unchanged (Figures 15, 17 and 19; chain and dotted lines). The fact that the levels of the transverse profiles of the normalised saturated modes are lower at the represented station results from the upstream shift of the maximum. We should expect, in accordance with the unconfined cylinder wake, to obtain the global maxima of the even streamwise and odd transverse velocity harmonics lying on the flow axis.[24] Figure 18 shows that for the fourth harmonic of the streamwise velocity the maximum of the slave mode belongs to the lateral lobe. This particularity can be attributed to the sharp edges of the obstacle. At saturation the same harmonic has already the expected structure (see Figure 23) with the dominant central lobe. As a result, the maximum of the slave mode does not correspond to the same lobe as that of the saturated one. If only the central lobe is taken into account, the upstream shift of the maximum, however, subsists. The maximum moves from $x = 1{\cdot}75$ to $1{\cdot}62$ (see Table II).

The normalization (45) using a measure of the size of the fundamental appears to yield a satisfactory estimate of the relative sizes of individual harmonics in the whole domain of magnitude of the parameter $A(s)$. This can be seen in Table II, where the maximum values of all computed modes normalized via (45) and (39) are given. These maxima appear to be all of the order of unity. This means that the Fourier decomposition (11) has roughly the convergence of a geometrical series with $A(s)$ as the quotient. The found value $A(\infty) = 0{\cdot}156$ explains its rapid convergence.

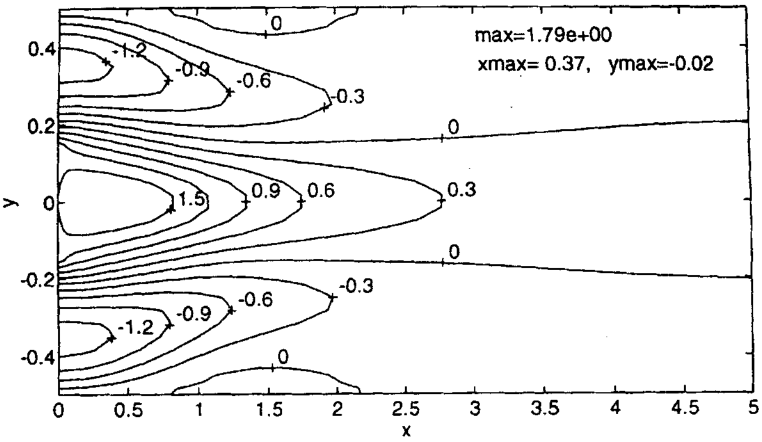

Figure 20. Iso-velocity contours of mean u-velocity deficit at saturation

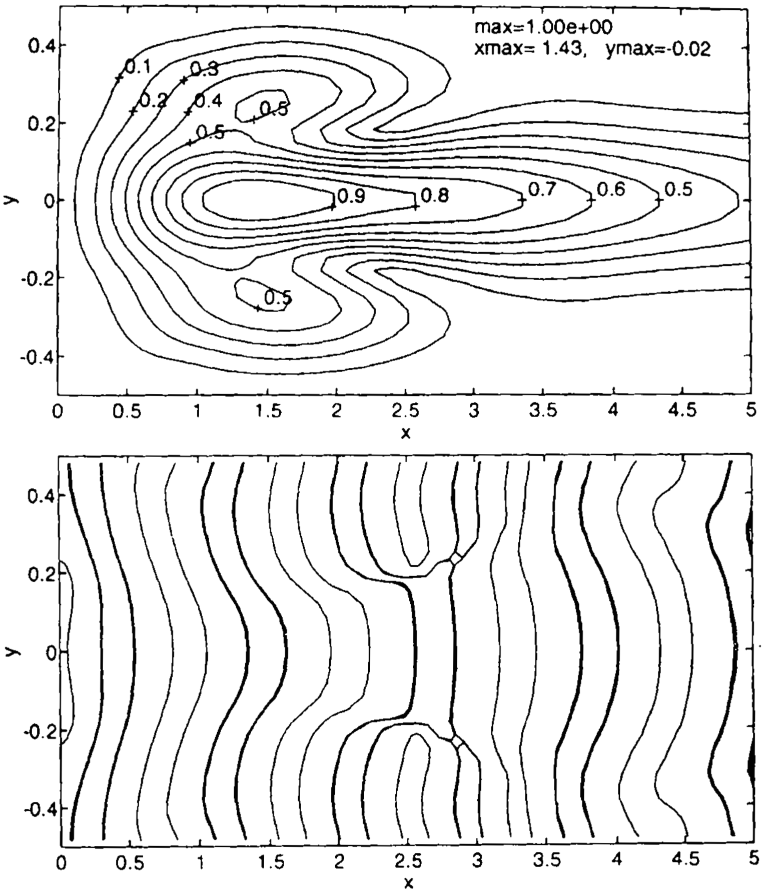

Figure 21. Iso-amplitude (top) and iso-phase (bottom) charts of transverse v-velocity component of normalized fundamental at saturation

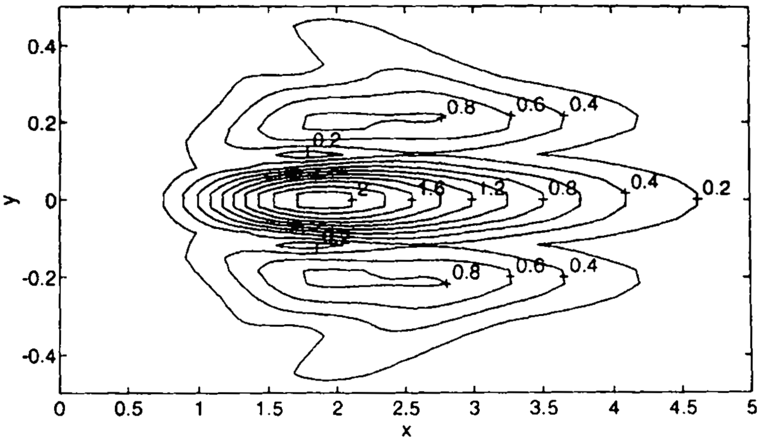

Figure 22. Iso-amplitude chart of streamwise u-velocity component of normalized second ($n = 2$) Fourier mode at saturation. For normalization see caption of Figure 14

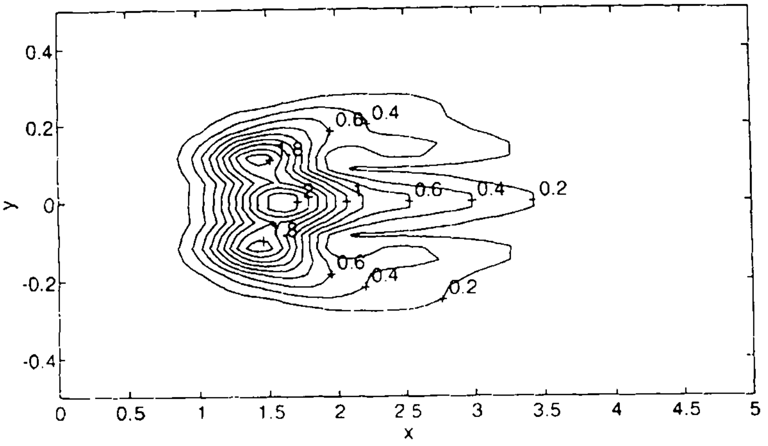

Figure 23. Iso-amplitude chart of streamwise u-velocity component of normalised fourth ($n = 4$) Fourier mode at saturation. For normalization see caption of Figure 14

The normalized mean value correction was also included in Table II. It was obtained by subtracting the basic flow from the mean flow. The normalized maximum for the streamwise velocity component appears to be substantially higher than for other normalized modes (about 10–11·5 as compared with about 1–3). Almost the same value found for the linear regime and at saturation confirms the second-order magnitude of this correction.

The high level of the mean value correction of the streamwise velocity results in a spectacular modification of the mean flow due to the instability development, in particular in an unconfined wake and for higher Reynolds number values.[23] However, even in the presented confined case the mean value correction leads to a relatively significant deformation of the mean flow (see Figures 7 and 20). The mean value correction being primarily a result of the coupling between the mean value and the fundamental (see equation (41)), it can be concluded that this coupling will be essential for the non-linear effects of the instability. This conclusion was further confirmed by the analysis of the numerical accuracy of the Fourier development in Reference 19, which showed that the saturation could be obtained by taking into account merely the coupling of the first harmonic with the mean value. The coupling with the second harmonic in (41) appeared to lower the amplitude of the fundamental only by less than 2%.

Table II. Positions of maxima and maximum values of normalized modes (45)

	Slave modes						Saturated modes					
	$\tilde{a}_0$	a_1	a_2	a_3	a_4	a_5	$\tilde{a}_0$	a_1	a_2	a_3	a_4	a_5
$a_{n,u,\max}$	10·36	1·51	2·06	2·18	1·48*	1·97	11·47	1·41	2·07	2·06	2·11	2·10
$x_{\max}$	2·25	1·95	2·02	1·81	1·75*	1·49	2·17	1·74	1·88	1·68	1·62	1·37
$y_{\max}$	0·00	−0·10	0·00	−0·07	0·00*	−0·07	0·00	0·10	0·00	−0·17	0·00	−0·17
$a_{n,v,\max}$	0·67	1·00	1·67	2·56	3·29	3·05	0·91	1·00	1·69	3·08	3·26	2·81
$x_{\max}$	0·89	1·75	2·10	2·02	1·81	1·62	0·79	1·43	2·02	1·88	1·62	1·43
$y_{\max}$	0·17	0·00	−0·10	0·00	−0·101	−0·10	0·17	0·00	−0·10	0·00	−0·07	−0·10

* Maximum of streamwise profile along flow axis ($y = 0$).

In Figures 9, 11, 14–18 and 21 we represented also the iso-phase charts. These charts make it possible to estimate the local wavelength (by measuring the spatial distance between successive corresponding iso-phase lines). It appears that the wavelength varies throughout the domain for each harmonic. On one hand the wavelength is shorter along the solid wall, bringing about phase dislocations even for the fundamental harmonic; on the other hand, e.g. in Figure 21, it increases downstream of the obstacle along the flow axis up to about $x = 2{\cdot}5$ and starts to decrease beyond this station. The comparison of the charts for various harmonics shows that, except close to the obstacle, at a given point of the flow the local wave number of the nth harmonic is quite accurately proportional to n times the local wave number of the fundamental, which means that each point of the flow is characterized by roughly the same phase velocity for all harmonics. These properties can be analysed more accurately by computing local wave numbers using the formula

$$\vec{k}_{n,u} = -\nabla\varphi_{n,u} = \nabla\ \mathrm{Im}(\ln c_{n,u}),$$

where the index n, u refers to the streamwise component of the nth harmonic and $\varphi_{n,u}$ stands for its phase. In the same way we can define the local wave number $\vec{k}_{n,v}$ relative to the v-component. The local phase velocity is obtained by dividing the angular frequency ω by the local wave number. According to what we have said about the wavelength, the phase velocity is smaller in the near wake and grows slightly downstream (see Figure 24) along the flow axis in the interval $0 < x < 2{\cdot}5$. For our nearly critical Reynolds number the variation in the wave number due to saturation is relatively small (about 1·3% on average and 4·5% at $x = 5$). These variations are partially compensated by the 1·06% increase in the angular velocity (see Figure 25) to yield an average phase velocity variation of only 0·2%.

Let us remark that the fact that the local phase velocity is almost the same for all harmonics, except immediately downstream of the obstacle, sets a very physical constraint on the spatial resolution of the flow field. Assessment of the obtained convergence rate of the series (11) presented in Reference 19 or based on Table II and the level of the fundamental shows that accounting for more than five harmonics would bring corrections well below the machine accuracy. This is due to the low, nearly critical, Reynolds number. For higher Reynolds numbers the saturation value $A(\infty)$ of the order parameter of the bifurcation increases, making the convergence slower. This might lead to the

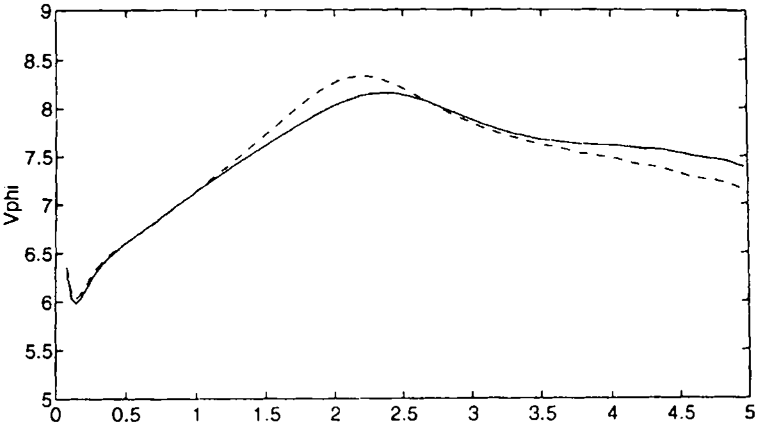

Figure 24. Phase velocity along flow axis for transverse component of fundamental harmonic for small amplitudes (full line) and at saturation (broken line)

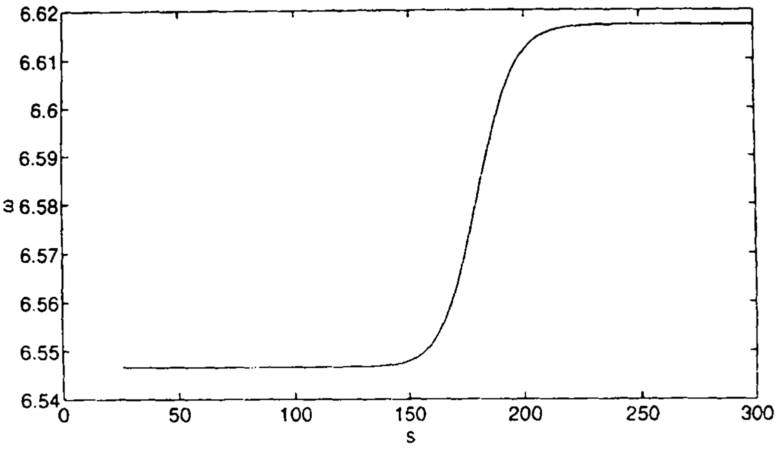

Figure 25. Time evolution of local angular velocity at point (1·04, 0·0)

necessity to account for a higher number of harmonics if a high precision is sought. (Actually, in the unconfined cylinder wake the characteristic value of $A(\infty)$ was found[24] to be as high as about 0·4 at more than twice the critical Reynolds number.) Neglecting harmonics higher than $n = 5$ yields then an error of about 0·6%. If a better accuracy is sought and more harmonics, say N, are to be taken into account, it has to be noted that the spatial resolution must be sufficient to capture the wavelength of the highest of them, which is N times smaller than that of the fundamental. In our case the wavelength of the saturated fundamental was found to be 1·12 at $x = 5$. As a result, the wavelength of the fifth harmonic is about 0·22, whereas the step of discretization of the x-co-ordinate increases from 0·032 to reach 0·13 at this place ($x = 5$) of the computational domain and the fifth harmonic is badly resolved so far from the obstacle.

4.6.2. Saturation process. The onset of the saturation process occurs simultaneously on all harmonics as can be seen in Figure 13. If we define the onset of saturation on the nth harmonic by a 1% decrease in the amplification rate divided by n with respect to the linear value γ and the completion of saturation as reaching 99% of the saturation value, we find the saturation process to set in at $s \approx 145$ and to end at $s \approx 215$, i.e. to last about 70 dimensionless time units. The so-defined onset of saturation occurs when the parameter $A(s)$ reaches roughly 10% of the saturation value $A(\infty) = 0{\cdot}156$.

Another quantity displaying the same behaviour is the instantaneous angular velocity ω appearing in (12). The period correction being defined at a selected point $\vec{x}_0$, ω represents, strictly speaking, the local angular velocity at this point. The local instantaneous corrections with respect to this value are, however, very small. The time evolution of the angular velocity has been represented in Figure 25. It shows the same time interval corresponding to the saturation process as the amplification rates. Let us recall the difficulty of extracting the initial linear value ω_0 from a direct simulation (Figure 5). In this case the constant value corresponding to the linear regime is clearly visible and allows us to obtain the increase in angular velocity $\Delta\omega$ due to non-linear effects very accurately: $\Delta\omega = 0{\cdot}0703$. The trend of the angular velocity to increase is due to the supercritical nature of the bifurcation.

The form of the modes is also sensitive to the onset of saturation. Indeed, knowing that the modes are rigid both for small amplitudes and at saturation, we can define the saturation time interval also as that corresponding to 99% of the streamwise shift of the maximum of the modulus corresponding to a

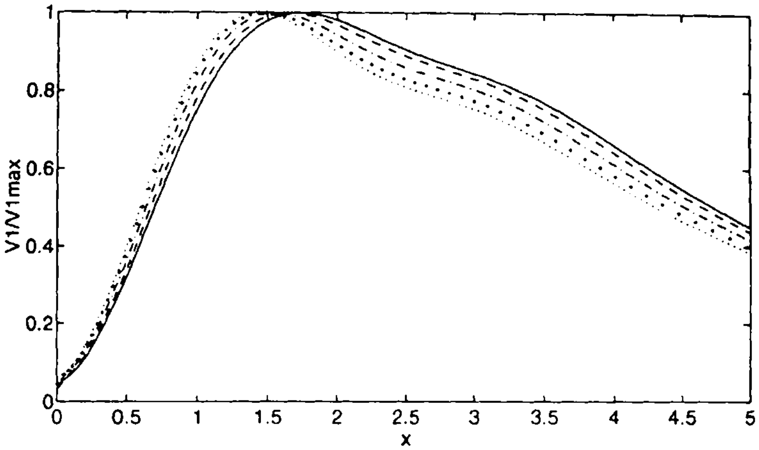

Figure 26. Evolution of streamwise profile of fundamental of transverse v-velocity during saturation process: full lines, $s = 150$; broken line, $s = 170$; chain line $s = 180$; large-dotted line, $s = 190$; small-dotted line, $s = 210$

given component and harmonic. That is, if Δx is the total shift of the maximum in the upstream direction, the onset of saturation corresponds to $x_{\mathrm{max}} = x_{\mathrm{max,small}} - 0{\cdot}01\Delta x$ and its completion corresponds to the maximum position reaching the value $x_{\mathrm{max}} = x_{\mathrm{max,sat}} + 0{\cdot}01\Delta x$, with $x_{\mathrm{max,small}}$ standing fro the maximum of the infintesimal mode and $x_{\mathrm{max,sat}}$ for the maximum at saturation. Then the time interval characterizing the saturation extends from $s \approx 144$ to 213 (see Figures 26 and 27).

Another interesting issue is the uniformity of 'instantaneous' and 'local' angular velocities of the flow oscillations. We have seen that the Fourier coefficients $\mathbf{c}_n$ or their normalized counterparts $\mathbf{a}_n$ were able to accommodate deviations with respect to the angular velocity appearing in the Fourier decomposition (11). These deviations are described by the angular velocity of the computed modes in the complex plane and can be expressed as vector functions of the space position with components corresponding to both components of the harmonics. At saturation, equations (12) completed by the period correction procedure (22) become steady and thus the Fourier coefficients no longer rotate. As a consequence, the flow oscillations obtained are, in accordance with direct simulation results,[15]

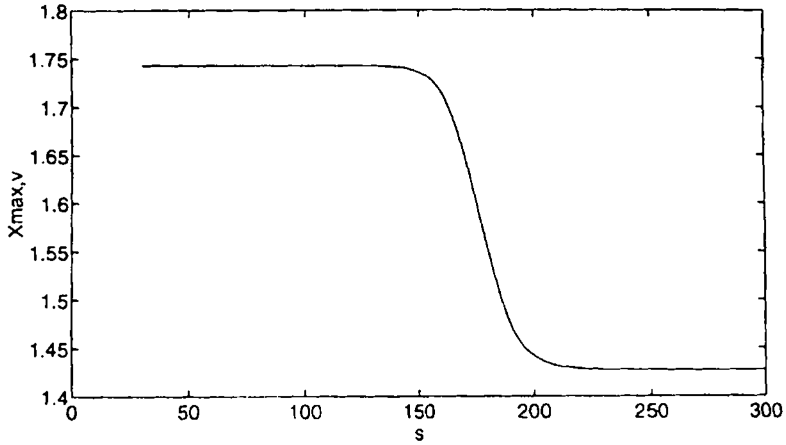

Figure 27. Time evolution of x-co-ordinate kof maximum of v-velocity component of fundamental harmonic

characterized by a period which is uniform throughout the flow. Its value is expressed by ω appearing in (12) and obtained by the period correction (22). The same was shown to hold for small amplitudes where the system (12) is unsteady but where the time dependence could be extracted via the renormalization (31), (32). During the saturation process the local angular velocities vary in space from component to component and from one harmonic to another. In order not to overburden the paper with too many figures, we do not present the corresponding chart. We found the angular velocity of e.g. the v-velocity component of the fundamental ($c_{1,v}$ at a time corresponding to the middle of the saturation process to vary in space within about 0·5% of the angular velocity increase $\Delta\omega = \omega_{\text{sat}} - \omega_0$ due to saturation. The local angular velocity was found to decrease in the downstream direction, which means that the saturation process sets in more slowly farther downstream of the obstacle. This conclusion is confirmed by an analogous analysis of local growth rates and by direct simulation results.

4.6.3. Validity of the Landau model. Let us consider again the simplified system (40)–(42). If we assume, in accordance with Reference 15, that the mode deformation described by $\partial\mathbf{a}_1/\partial s$ is much slower than its amplification, we can neglect this derivative in (41) and assume that the form $\mathbf{a}_1$ does not differ very much from $\mathbf{a}_{1,\text{lin}}$. We can then denote the complex Landau constant relative to a given velocity component (here e.g. v) at a fixed point $\vec{x}_0$ as

$$\frac{C^{(v)}(\vec{x}_0) = [\mathbf{B}(\mathbf{a}_2, \mathbf{a}_1) + \mathbf{B}(\mathbf{a}_1, \mathbf{a}_2) + \mathbf{B}(\tilde{\mathbf{a}}_0, \mathbf{a}_1) + \mathbf{B}(\mathbf{a}_1, \tilde{\mathbf{a}}_0)]_{v,\vec{x}_0}}{a_{1,v}(\vec{x}_0),} \tag{46}$$

where we have stressed the component and position dependence.[15] The real part of (41) then gives

$$\frac{1}{A(s)}\frac{\mathrm{d}A(s)}{\mathrm{d}s} = \gamma - C_\mathrm{r}^{(v)}(\vec{x}_0)A_2(s) \tag{47}$$

and the imaginary part gives

$$\omega = \omega_0 - C_\mathrm{i}^{(v)}(\vec{x}_0)A^2(s), \tag{48}$$

where $C_\mathrm{r}^{(v)}$ and $C_\mathrm{i}^{(v)}$ stand respectively for the real and imaginary parts of the Landau constant. We thus arrive at the well-known local Landau-like[6] behaviour which is known to model the saturation of amplitudes, i.e. the fact that the amplitude and angular velocity of wake oscillations tend to constant values.[4–6,15] The local interpretation of the Landau model for wakes has been discussed in Reference 15.

The Landau constants can be determined from the saturation amplitude and angular frequency (equations (47) and (48)) so that the model is (trivially) exactly satisfied for small amplitudes and at saturation. The issue of the Landau model validation consists of verifying the linearity of the RHSs of (47) and (48) as functions of $A^2(s)$. In Reference 15 we have shown that the Landau model is rather well-satisfied near the threshold at any fixed point of the flow, but we pointed out that the deviations from the Landau model are visible even at low Reynolds numbers. These deviations are caused by the deformation of the mode contradicting the assumption leading to the Landau model. The knowledge of the instantaneous values of the amplitudes and angular frequencies of the wake fundamental at all points of the flow allows us to investigate equation (48) and to see how the Landau-like behaviour is satisfied in time and in space.

It appears that farther downstream (at $x = 5$) and on the flow axis the Landau model (47), (48) underpredicts the instantaneous non-linear correction of angular frequency in the middle of the saturation process ($s \approx 180$) by as much as 20%. Upstream, near the obstacle, the growth of the mode is more rapid and, as the gradient between the obstacle and the maximum of the normalized mode becomes steeper (see Figure 26), the mode deformation appears to be able to compensate the difference with respect to the Landau model prediction. Quite near the obstacle (for $x < 1$) the Landau model is found to overpredict the angular velocity correction by about 3% in the middle of the saturation process. At $x = 1$ the angular velocity equation of the Landau model is almost exactly satisfied. However, the amplitude equation (47) is not satisfied at this point, so that no point where both equations were satisfied could be found.

In spite of this conclusion, we have seen that it is possible to fit the Landau model constants so as to make the model exact for very small amplitudes (in the domain of the exponential growth of rigid modes) and at saturation. As a result, some Landau model parameters keep their rigorous physical significance. This issue has been addressed in more detail in Reference 15, so it is sufficient to give the values of these constants found here. Firstly, equation (47) and (48) contain of course the linear eigenvalue given by (28). The constant (46) has been shown to be specific for a given position and component; however, the normalized Landau constant C_i/C_r has been recognized (e.g. References 5, 10 and 20) as a relevant characteristic. Taking into account that[15] (see equation (47) and (48))

$$C_i/C_r = -\Delta\omega/\gamma,$$

$\Delta\omega$ being the increase in the angular velocity due to non-linear effects, the normalized Landau constant is a global characteristic.

In our case the normalized Landau constant assumes the value

$$C_i/C_r = -1{\cdot}0068. \tag{49}$$

To give an idea of the potential (without account of the spatial discretization errors) precision of the determination of this constant by our method, let us note that the angular velocities of the Fourier components (11) were found to be very accurately zero not only at saturation (where the whole decomposition is steady) but also for small amplitudes (interval of constant growth rates). As a result, the time discretization errors are only of a spectral character and should not thus be higher than 10^{-5} as far as the determination of the value $\Delta\omega$ is concerned. As a result, a similar error estimate can be set for the value (49). This is to be compared with direct numerical results (an error of about 3% was obtained in Reference 15) or with experimental measures (16%[17]). The error of the normalized Landau constant is thus entirely controlled by the spatial discretization (about 1%).

5. CONCLUSIONS

In this paper we have addressed the point of the physically relevant characterization of the Bénard–von Kármán instability. The same issue was discussed already in our previous works in the context of the Landau model interpretation[15] and of the description of the symmetry conservation at the Hopf bifurcation. It has been shown that the well-known symmetry breaking can be interpreted as a transition to a more complex group representation of the corresponding symmetry group (the y-coordinate inversion in a symmetric 2D wake). This group representation was found to be defined by the same set of Fourier components as that used in this paper.

The present numerical study gives further, more general, support to the physical relevance of the Fourier modes of the wake. It shows that the Bénard–von Kármán instability can be mathematically accurately and physically correctly described by the set of its time Fourier components considered as functions in space slowly varying in time. The basic theoretical concept of the present Fourier mode description is a natural extension of linear and weekly non-linear theory and provides a continuous link between linear theory and a full Navier–Stokes description. We have shown that it can account for all known non-linear effects observed in wakes. It is sufficiently general to be able to accommodate all wake configurations, the geometry (3D, symmetries, boundary conditions) being a matter of the spatial description which can be implemented arbitrarily. Though we have not submitted our theory to tests for other cases of the Hopf bifurcation, we believe it applies to Hopf bifurcations in general, at least not too far from the threshold.

For the first time it has been possible to follow the pertinent characteristics of the instability from the onset until saturation. Though weakly non-linear theories[8] allow one to predict qualitatively the existence of slave modes[9] at the onset of the instability, these higher-order modes have never been computed before in a fully 2D case. The amplification rate and the detailed spatial structure of the slave modes have, moreover, been followed in a continuous way all the time from the linear regime until saturation in this paper.

Not only could some expected, but never rigorously proved, properties such as those of the linear regime amplification rates of higher harmonics could be confirmed, but also several new results of practical and theoretical importance have been obtained. The most important are the determinant role of the coupling of the fundamental with the mean value for the saturation providing a physically more accurate alternative for a qualitative modelling of the instability than the widely used Landau model, the determination of the level corresponding to the onset of saturation setting the limit to linear theory, the estimation of the convergence properties of the Fourier decomposition having important numerical implications and the accurate computation of the angular velocity increase giving access to the normalized Landau constant.

Apart from its theoretical relevance, the Fourier mode representation proves a natural and extremely accurate spectral representation for a numerical description of the wakes. This description allows us to use any space discretization method for the modes and obtain a highly efficient, spectrally accurate time discretization. The latter being easily made more accurate than the spatial one, the method enables us to fully exploit the possibilities of the spatial solver. Physical considerations concerning the wavelengths of harmonics provide a very simple tool for balancing the spatial and temporal discretization accuracy.

ACKNOWLEDGEMENTS

Gilles Carte wishes to thank the Electricité de France Service RNE-TTA for the three-year Ph.D. grant no. T37 L09 to support this work.

Jan Dušek wishes to thank the French Ministère de l'Enseignement Supérieur et de la Recherche for the visiting professor's position at the Institut de Mécanique Statistique de la Turbulence in Marseilles in the framework of which the present work has been carried out.

REFERENCES

1. L. S. G. Kovasznay, *Proc. R. Soc. Lond. A*, **198**, 194 (1949). A. Roshko, *NACA Rep 1191*, 1954. M. Coutanceauy and R. Bouard, *J. Fluid. Mech.*, **79**, 231 (1977). M. Coutanceau and R. Bouard, *J. Fluid. Mech.*, **79**, 257 (1977). C. H. K. Williamson, *J. Fluid. Mech.*, **206**, 579 (1989).
2. G. E. Mattingly and W. O. Criminale, *J. Fluid. Mech.*, **51**, 233 (1972). R. T. Pierrehumbert, *J. Atmos. Sci.*, **41**, 2141 (1984). W. Koch, *J. Sound Vibr.*, **99**, 53 (1985). G. S. Triantafyllou, M. S. Triantafyllou and C. Chryssostomidis, *J. Fluid. Mech.*, **170**, 461 (1986). P. A. Monkewitz, *Phys. Fluids*, **31**, 999 (1988). X. Yang and Z. Zebib, *Phys. Fluids A*, **1**, 689 (1989). J. M. Chomaz, and P. Huerre and L. G. Redekopp, *Stud. Appl. Math.*, **84**, 119 (1991).
3. K. Hannemann and H. Oertel Jr., *J. Fluid. Mech.*, **199**, 55 (1989).
4. C. Mathis, M. Provansal and L. Boyer, *J. Fluid Mech.*, **182**, 1 (1987).
5. P. J. Strykowski and K. R. Sreenivasan, *J. Fluid Mech.*, **218**, 71 (1990).
6. L. D. Landau and F. M. Lifshitz, *Fluid Mechanics, Course of Theoretical Physics*, Vol. 6, Pergamon, New York, 1959.
7. K. Stewartson and J. T. Stuart, *J. Fluid Mech.*, **48**, 529 (1971).
8. T. Herbert, *J. Fluid Mech.*, **126**, 167 (1983).
9. P. Manneville, *Dissipative Structures and Weak Turbulence*, Academic Press, San Diego, CA, London, UK, 1990.
10. S. Raghu and P. A. Monkewitz, *Phys. Fluids A*, **3**, 501 (1991).

11. J. Dušek, Ph. Fraunié and P. Le Gal, *Phys. Fluids*, **6**, 172 (1994).
12. C. P. Jackson, *J. Fluid Mech.*, **182**, 23 (1987).
13. M. Braza, P. Chassaing and H. Ha Minh, *J. Fluid Mech.*, **165**, 79 (1986).
14. G. E. Karniadakis and G. S. Triantafyllou, *J. Fluid Mech.*, **199**, 441 (1989).
15. J. Dušek, P. Le Gal and Ph. Fraunié, *J. Fluid Mech.*, **264**, 59 (1994).
16. F. P. Bertolotti, Th. Herbert and P. R. Spalart, *J. Fluid Mech.*, **242**, 441 (1992).
17. M. Schumm, E. Berger and P. Monkewitz, *J. Fluid Mech.*, **271**, 17 (1994).
18. S. Goujon-Durand, P. Jenffer and J. E. Wesfreid, *Phys. Rev. E*, **50**, 1 (1994).
19. G. Carte, J. Dušek and Ph. Fraunié, *J. Comput. Phys.*, **120**, 171 (1995).
20. T. Leweke and M. Provansal, *J. Fluid Mech.*, **288**, 265 (1995).
21. G. Jin and M. Braza, *J. Comput. Phys.*, **107**, 239 (1993).
22. V. Corquette and H. Williams, *Physica D*, **37**, 300 (1989).
23. J. Dušek, to appear in *Eur. J. Mech. B/Fluids*, **15**, (1996).
24. J. Dušek and Ph. Fraunié, *Proc. 8th Int. Conf. on Numerical Methods in Laminar and Turbulent Flow*, Pineridge Press, Swansea, UK, July 1993, pp. 15–25.